The Astrophysical Journal, 954:147 (19pp), 2023 September 10 https://doi.org/10.3847/1538-4357/acea7d

The Role of Pickup Ions in the Interaction of the Solar Wind with the Local Interstellar Medium. I. Importance of Kinetic Processes at the Heliospheric Termination Shock

R. K. Bera[1], F. Fraternale[1], N. V. Pogorelov[1,2], V. Roytershteyn[3], M. Gedalin[4], D. J. McComas[5], and G. P. Zank[1,2]
[1] Center for Space Plasma and Aeronomic Research, The University of Alabama in Huntsville, Huntsville, AL 35899, USA; rkb0019@uah.edu
[2] Department of Space Science, The University of Alabama in Huntsville, Huntsville, AL 35899, USA
[3] Space Science Institute, Boulder, CO 80301, USA
[4] Department of Physics, Ben-Gurion University of the Negev, Beer-Sheva, Israel
[5] Department of Astrophysical Sciences, Princeton University, Princeton, NJ 08544, USA
Received 2023 May 31; revised 2023 July 23; accepted 2023 July 24; published 2023 September 1

Abstract

The role of pickup ions (PUIs) in the solar wind interaction with the local interstellar medium is investigated with 3D, multifluid simulations. The flow of the mixture of all charged particles is described by the ideal MHD equations, with the source terms responsible for charge exchange between ions and neutral atoms. The thermodynamically distinct populations of neutrals are governed by individual sets of gas dynamics Euler equations. PUIs are treated as a separate, comoving fluid. Because the anisotropic behavior of PUIs at the heliospheric termination shocks is not described by the standard conservation laws (a.k.a. the Rankine–Hugoniot relations), we derived boundary conditions for them, which are obtained from the dedicated kinetic simulations of collisionless shocks. It is demonstrated that this approach to treating PUIs makes the computation results more consistent with observational data. In particular, the PUI pressure in the inner heliosheath (IHS) becomes higher by ∼40%–50% in the new model, as compared with the solutions where no special boundary conditions are applied. Hotter PUIs eventually lead to charge-exchange-driven cooling of the IHS plasma, which reduces the IHS width by ∼15% (∼8–10 au) in the upwind direction, and even more in the other directions. The density of secondary neutral atoms born in the IHS decreases by ∼30%, while their temperature increases by ∼60%. Simulation results are validated with New Horizons data at distances between 11 and 47 au.

Unified Astronomy Thesaurus concepts: Heliosphere (711); Solar wind (1534); Interstellar medium (847); Pickup ions (1239); Termination shock (1690); Magnetohydrodynamics (1964); Space plasmas (1544); Charge-exchange ionization (2056)

1. Introduction

The heliosphere is a part of the interstellar space carved out by the solar wind (SW) emanating from the Sun. The shape of the heliosphere is determined by the SW interaction with the partially ionized local interstellar medium (LISM). From a magnetohydrodynamics (MHD) perspective, the boundary between the SW and LISM plasmas is a tangential discontinuity known as the heliopause (HP). Collision of the supersonic SW with the HP results in a heliospheric termination shock (TS). Both the TS and HP were identified in situ by the Voyager 1 (V1) and Voyager 2 (V2) spacecraft. The region between TS and HP is commonly called the inner heliosheath (IHS), or simply the heliosheath. The LISM plasma flow is known to be supersonic, but it can be subfast magnetosonic if the interstellar magnetic field (ISMF) is sufficiently strong. The factors that affect the presence (or absence) of the so-called bow shock (BS) in front of the HP are discussed by McComas et al. (2012), Zank et al. (2013), and Pogorelov et al. (2017b). Unlike charged particles, the interstellar neutral (ISN) atoms, which predominantly consist of hydrogen, easily cross the HP and enter the heliosphere where, through ionization and charge exchange, they give birth to so-called pickup ions (PUIs). Once created, PUIs respond to the motional electric field instantaneously and start to move outward with the SW, acquiring its bulk speed (Parker 1965). Models indicate that newly born PUIs rapidly scatter onto a bispherical, or even more isotropic, distribution function, which becomes filled as PUIs advect with the SW (e.g., Lee & Ip 1987; Galeev & Sagdeev 1988; Williams & Zank 1994; Zank 1999, 2015; Isenberg et al. 2003, 2010, 2023; Isenberg 2005). A recent review of this topic has been presented by Isenberg et al. (2023).

As observed by Voyager 2 and New Horizons (NH; see, e.g., Richardson et al. 1995; Richardson & Smith 2003; Decker et al. 2008, 2015; McComas et al. 2017, 2021), and shown by theoretical models and simulations (e.g., Wallis 1971; Vasyliunas & Siscoe 1976; Zank 1999; Malama et al. 2006; Zank et al. 2014, 2018; Kim et al. 2016, 2018; Pogorelov et al. 2016), the increase in PUI density with heliocentric distance and their high temperature ($\sim 10^7$ K) ultimately cause the PUI pressure to dominate the thermal SW pressure and magnetic pressure in the region of space that is conventionally called the outer heliosphere. At heliocentric distances exceeding the ionization cavity, the waves generated during the process of isotropization of the PUI distribution interact with the turbulence cascade that ultimately heats the thermal SW protons (e.g., Williams et al. 1995; Zank et al. 1996a, 2018; Matthaeus et al. 1999; Smith et al. 2001, 2006; Isenberg et al. 2003; Chalov et al. 2006; Gamayunov et al. 2012). As newly born PUIs extract energy from the kinetic energy of the SW, the bulk speed of the ion mixture decreases.

The mean time between collisions of PUIs and thermal protons in the outer heliosphere is approximately three orders of magnitude larger than the convection time of SW from 10 to

100 au. Assuming the electron temperature to be equal to the proton temperature, the PUI–electron collisional mean free time is still ∼20–30 times larger. For this reason, PUIs do not achieve thermodynamic equilibrium with the thermal SW, and they constitute a distinct suprathermal ion component (Isenberg 1986; Zank et al. 2014). PUIs were discovered in situ and described by Möbius et al. (1985) and Geiss et al. (1994). PUIs themselves can undergo charge exchange producing energetic neutral atoms (ENAs). As the properties of ENAs are strongly affected by the properties of PUIs, ENA measurements such as from the Interstellar Boundary Explorer (IBEX; McComas et al. 2009a) detector make it possible to study the global heliosphere remotely (McComas et al. 2009b; Heerikhuisen et al. 2010; Reisenfeld et al. 2021; Zirnstein et al. 2022).

Numerical modeling is a powerful tool for understanding the three-dimensional features of the SW–LISM interaction and interpreting in situ measurements performed by Voyagers and NH, and remote observations by IBEX (see, e.g., Pogorelov et al. 2017a; Fraternale et al. 2022; Kleimann et al. 2022; Sokół et al. 2022; Zank et al. 2022; Pogorelov 2023). Development of new mathematical models of the SW–LISM interaction in the presence of PUIs is especially important in the anticipation of new, higher-resolution data to be provided by future space missions, such as Interstellar Mapping and Acceleration Probe (IMAP; McComas et al. 2018).

Even if PUIs are not treated separately from the thermal ions, the charge-exchange source terms in the gas dynamics/MHD equations describing the flow of SW plasma automatically ensure their presence (Baranov & Malama 1993; Zank et al. 1996c; Linde et al. 1998; Pogorelov et al. 2006). However, the single plasma fluid models assume immediate assimilation of PUIs into a single Maxwellian distribution with the thermal SW, which is (i) not accurate and (ii) makes it impossible to determine the properties of individual plasma components. Ensuring a proper energy separation between PUIs and thermal ions is important not only because the flow topology is strongly affected by charge exchange, which is different for different populations of ions, but also because the properties of PUIs and ENAs are strongly correlated. Besides, the V2 plasma instrument (the V1 plasma instrument is not operational) measures the properties of the thermal protons only, which makes simulations essential for comparison with the Voyager observational data. Isenberg (1986) was the first to show that the effect of nonthermal PUIs on the SW–LISM interaction can be quantified if they are treated separately from the thermal SW ions.

While a number of global, three-dimensional, MHD models of the SW–LISM interaction exist in which PUIs are treated separately (e.g., Kryukov et al. 2012; Pogorelov et al. 2016; Usmanov et al. 2016; Opher et al. 2020), none takes into account the complicated kinetic processes that accompany the behavior of PUIs crossing collisionless shocks, such as the TS (see, e.g., Gedalin et al. 1995, 2016, 2021a, 2021b, Gedalin 2022; Zank et al. 1996b, 2010a; Chalov & Fahr 2000; le Roux et al. 2007; Burrows et al. 2010; Ariad & Gedalin 2013; Kumar et al. 2018; Matsukiyo et al. 2019; Giacalone et al. 2021). A fluid approach is not appropriate for this purpose, because PUIs can be reflected upstream at the shock front and gain energy until they finally cross the shock. The reflection of thermal, cold SW ions is much less efficient, and PUIs experience preferential heating across the TS (Zank et al. 1996b, 2010a; Richardson et al. 2008). Because of these processes, the PUI distribution function in the TS vicinity becomes highly anisotropic, even in the SW frame (Zank et al. 1996b; Chalov et al. 2015; Gedalin et al. 2021a). In principle, a detailed kinetic analysis is necessary to acquire a more realistic understanding of the PUI behavior across shocks. However, due to prohibitive computational costs and the complexity of such kinetic approaches, various fluid models of PUIs are used (Pogorelov et al. 2016; Usmanov et al. 2016; Opher et al. 2020). All numerical simulations of the three-dimensional global SW–LISM interactions performed so far with a separate treatment of fluid PUIs have used either simplified approaches (Pogorelov et al. 2016) or no special conditions at all (Usmanov et al. 2016; Opher et al. 2020) to describe the PUI behavior across the TS. It should be noted that the MHD Rankine–Hugoniot relations, which express the conservation of mass, momentum, energy, and magnetic flux at shocks, do not provide specific information on the behavior of PUIs.

In this paper, we use hybrid kinetic simulations to derive the boundary conditions (b.c.s) for PUIs at the TS and apply them in our modeling of the SW–LISM interaction. Hybrid simulations of the PUI transport through the TS are used to describe the energization of PUIs at the shock front. They include the kinetic processes of kinematic mixing and instabilities that lead to PUI isotropization behind the TS, thus providing us with the shock relations on the MHD scale. This approach allows us to treat PUIs as an individual fluid.

We have implemented these b.c.s in our Multi-Scale Fluid-Kinetic Simulation Suite (MS-FLUKSS), an adaptive mesh refinement (AMR) software that solves the ideal MHD equations coupled to the multifluid or kinetic transport models for neutral atoms (Pogorelov et al. 2006, 2014, 2016, 2017a, 2021; Borovikov et al. 2009, 2013; Heerikhuisen & Pogorelov 2011; Kryukov et al. 2012; Heerikhuisen et al. 2016, 2019; Kim et al. 2018). It is worth noting that these b.c.s are used only to treat the transmission of PUIs at the shock. We do not explicitly modify the properties of the plasma mixture (i.e., the mixture of all charged particles) at the TS, and assume that it is described well by the MHD system of conservation laws. This assumption is suitable at sufficiently long time scales (Zank et al. 2014; Zank 2015). Using the most recent consensus values for the LISM parameters (Zirnstein et al. 2016; Swaczyna et al. 2020; Zhang et al. 2020), the simulations are performed to obtain a global steady-state heliospheric solution.

As shown by Zilbersher & Gedalin (1997), the presence of a substructure within a shock ramp may provide additional acceleration to a fraction of reflected PUIs. Ariad & Gedalin (2013) analyzed this phenomenon at the TS, where V2 discovered a "sawtooth" structure in the magnetic field distribution inside the ramp and confirmed the effect of multiple reflections and surfing of PUIs caused by such a structure (see also Burrows et al. 2010). Zirnstein et al. (2021) elaborated on this acceleration mechanism and came to the conclusion that a suprathermal tail in the PUI distribution downstream of the TS would be consistent with the IBEX observations only if the turbulent fluctuations in front of and behind the TS are of the same intensity as inside the shock ramp. However, V2 observations revealed a much lower (∼10 times) turbulent activity. The hybrid kinetic simulations used in what follows include self-generated fluctuations without pre-existing upstream turbulence.

The structure of the paper is as follows. In Section 2, we present our physical model. The simulation setup and boundary

conditions used in this study are discussed in Section 3. The details of the b.c.s for PUIs at the TS and their implementation in the global model are described in Section 4. The simulation results and related discussion are given in Section 5, with a summary and conclusions presented in Section 6.

2. Physical Model

We build on the multifluid model of the SW-LISM interaction described by Pogorelov et al. (2016). In our new model, the plasma mixture consists of three comoving populations of charged particles: thermal protons, electrons, and PUIs. The plasma flow is described by the ideal MHD equations, which express the conservation laws for mass, momentum, total energy, and magnetic flux. We distinguish three populations of neutral hydrogen (H) atoms: population 1 (labeled as $H_{(1)}$) represents the H atoms of interstellar origin, while populations 2 and 3 (labeled as $H_{(2)}$ and $H_{(3)}$) represent the neutral atoms created in the IHS and supersonic SW, respectively. Each of these atom populations is born in thermodynamically distinct regions of the heliosphere and therefore they are described by separate sets of Euler equations (Zank et al. 1996c; Pogorelov et al. 2006). PUIs are treated as a separate fluid by solving the corresponding continuity and pressure equations. The system is written as follows:

Plasma mixture:

$$\frac{\partial \rho}{\partial t} + \nabla \cdot (\rho \boldsymbol{u}) = S_{\Sigma}^{\rho} = 0 \tag{1}$$

$$\frac{\partial \rho \boldsymbol{u}}{\partial t} + \nabla \cdot \left[\rho \boldsymbol{u}\boldsymbol{u} + p^{*}\boldsymbol{I} - \frac{1}{4\pi}\boldsymbol{B}\boldsymbol{B} \right] = \boldsymbol{S}_{\Sigma}^{m} \tag{2}$$

$$\frac{\partial E}{\partial t} + \nabla \cdot \left[(E + p^{*})\boldsymbol{u} - \frac{1}{4\pi}(\boldsymbol{B} \cdot \boldsymbol{u})\boldsymbol{B} \right] = S_{\Sigma}^{E} \tag{3}$$

$$\frac{\partial \boldsymbol{B}}{\partial t} + \nabla \cdot (\boldsymbol{u}\boldsymbol{B} - \boldsymbol{B}\boldsymbol{u}) = 0. \tag{4}$$

Neutrals:

$$\frac{\partial \rho_a}{\partial t} + \nabla \cdot (\rho_a \boldsymbol{u}_a) = S_a^{\rho} \tag{5}$$

$$\frac{\partial \rho_a \boldsymbol{u}_a}{\partial t} + \nabla \cdot (\rho_a \boldsymbol{u}_a \boldsymbol{u}_a + p_a \boldsymbol{I}) = \boldsymbol{S}_a^{m} \tag{6}$$

$$\frac{\partial E_a}{\partial t} + \nabla \cdot [(E_a + p_a)\boldsymbol{u}_a] = S_a^{E}. \tag{7}$$

PUIs:

$$\frac{\partial \rho_{\mathrm{PUI}}}{\partial t} + \nabla \cdot (\rho_{\mathrm{PUI}} \boldsymbol{u}) = S_{\mathrm{PUI}}^{\rho} \tag{8}$$

$$\frac{\partial p_{\mathrm{PUI}}}{\partial t} + \nabla \cdot (p_{\mathrm{PUI}} \boldsymbol{u}) + (\gamma - 1) p_{\mathrm{PUI}} \nabla \cdot \boldsymbol{u} = S_{\mathrm{PUI}}^{p} - S_{\mathrm{w}}. \tag{9}$$

Here, ρ, p, and $\boldsymbol{u}$ represent, respectively, the mass density, thermal pressure, and bulk velocity vector, of the plasma mixture. This means that $p = p_{\mathrm{p,th}} + p_{\mathrm{PUI}} + p_{\mathrm{e}}$, where $p_{\mathrm{p,th}}$, p_{PUI}, and p_{e} are the thermal pressures of the thermal SW protons, PUIs, and electrons, respectively. In addition, $p^{*} = p + \boldsymbol{B}^2/8\pi$ is the total pressure (the sum of thermal and magnetic pressures), $E = p/(\gamma - 1) + \rho \boldsymbol{u}^2/2 + \boldsymbol{B}^2/8\pi$ is the total energy density (includes the magnetic energy) of the plasma mixture, $\boldsymbol{B}$ is the magnetic field vector, and $\boldsymbol{I}$ is the identity tensor. We assume that the adiabatic index, denoted as γ, is equal to $5/3$ for all species. The subscripts Σ, a, and PUI are used to refer to the plasma mixture, neutral populations, and PUIs, respectively. The index a can have values $H_{(1)}$, $H_{(2)}$, and $H_{(3)}$ representing the corresponding neutral atom populations. The source terms on the right-hand side of the density, momentum, energy, and pressure equations, S^{ρ}, $\boldsymbol{S}^{m}$, S^{E}, and S^{p}, describe the contribution of charge exchange and photoionization. The latter process is negligible at distances considered in the paper. In general, the expressions for the source terms depend on the choice of charge-exchange processes occurring in the different regions of the heliosphere. The pressure source terms for each species s can be expressed in terms of the remaining source terms (Pogorelov et al. 2016; DeStefano & Heerikhuisen 2020; Fraternale et al. 2021):

$$S_s^{p} = (\gamma - 1)\left(S_s^{E} - \boldsymbol{u} \cdot \boldsymbol{S}_s^{m} + \frac{1}{2} u^2 S_s^{\rho} \right). \tag{10}$$

We subdivide the SW–LISM interaction space into three regions: Region 1 is filled with the LISM plasma. Region 2 indicates the IHS, the space between the HP and TS. Region 3 corresponds to the supersonic SW between the TS and the inner simulation boundary. In addition to Equations (3)–(9), a level-set equation is solved to correctly identify the position of the HP (Borovikov et al. 2011).

The charge-exchange processes considered in this study are described in the Appendix. The expressions for the source terms are constructed from Zank et al. (1996c) and Pogorelov et al. (2016). The analytical expressions for source terms are derived assuming Maxwellian distributions for the ions and neutral atoms (see Appendix). The cross sections for charge exchange between protons and H atoms are taken from Lindsay & Stebbings (2005). The effect of non-Maxwellian distributions (DeStefano & Heerikhuisen 2020) will be considered elsewhere. PUIs are also created by charge exchange in Region 2 (in the IHS), but their temperature is much closer there to the temperature of thermal ions than in Region 3. Therefore, for simplicity, we attribute them to thermal protons. Although this may affect the properties of thermal ions in the IHS, the contribution of PUIs to the plasma pressure remains dominant (Malama et al. 2006).

The electron density is calculated assuming the quasi-neutrality condition, $n_{\mathrm{e}} = n_{\mathrm{p,th}} + n_{\mathrm{PUI}} = n$, where n_{e}, $n_{\mathrm{p,th}}$, and n_{PUI} are the electron, thermal proton, and PUI number densities, respectively. The electron temperature is assumed to be equal to the temperature of thermal protons, $T_{\mathrm{e}} = T_{\mathrm{p,th}}$. An extensive discussion of the role of electrons has been provided recently by Fraternale et al. (2023). The thermal pressure of each species is determined using the equation of state, $p_s = n_s k_{\mathrm{B}} T_s$; where p_s, n_s and T_s are the pressure, number density, and temperature of species s, and k_{B} is the Boltzmann constant.

The density and pressure of the thermal SW protons are obtained as

$$\rho_{\mathrm{p,th}} = \rho - \rho_{\mathrm{PUI}}; \quad p_{\mathrm{p,th}} = \rho_{\mathrm{p,th}} \times \frac{p - p_{\mathrm{PUI}}}{2\rho - \rho_{\mathrm{PUI}}}. \tag{11}$$

A significant fraction of the thermal proton heating in SW is caused by PUI-generated turbulence (Williams et al. 1995; Matthaeus et al. 1999; Smith et al. 2001; Isenberg et al. 2003, 2010; Breech et al. 2008; Adhikari et al. 2015, 2016; Usmanov et al. 2016; Zank et al. 2018), as shown by V2 measurements (Richardson et al. 2008, 2022). A number of such models have already been implemented in MS-FLUKSS (Kryukov et al.

2012; Pogorelov et al. 2013, 2014, 2017a; Kim et al. 2018; Fraternale et al. 2022). The existing models, however, are not valid in Region 2, where compressible turbulence plays an important role (Fraternale et al. 2022). As we do not use any turbulent transport model, to mimic the anticipated heating of the thermal SW by PUIs, we adopt a simplified approach (see also Wang & Richardson 2001; Usmanov & Goldstein 2006), where the source term in Equation (9) is decreased by 5%, i.e., $S_w = 0.05 S^p_{PUI}$, which automatically implies that the thermal plasma is heated by this amount. The fraction of energy to be transferred to thermal protons is adjusted to make their temperature closer to that in V2 data, as will be discussed in more detail in Section 5. We note that this is done only in the supersonic SW, and no changes are made to the source terms in the equations for the plasma mixture.

It is also worth noting that we do not need separate equations for the thermal protons, as in Usmanov et al. (2016). Their properties can be derived from those of the mixture and PUIs. Our approach is stipulated by the necessity to resolve the TS and HP with minimal numerical smearing, which can be achieved only if the equations are solved in the conservation-law form.

In this paper, we use stationary boundary conditions in the SW and LISM, so a steady state is obtained by solving the system of equations as $t \to \infty$.

3. Simulation Setup and Boundary Conditions

3.1. Simulation Setup

Equations (1)–(9) are solved numerically using MS-FLUKSS, which incorporates a hierarchy of physical models relevant to the SW–LISM interaction (Pogorelov et al. 2009b, 2010, 2014, 2017a, 2021; Pogorelov 2023, and references therein). PUIs are treated as a separate comoving fluid.

We solve the system of equations in a Cartesian coordinate system on a spherical grid with $192 \times 96 \times 64$ cells along the radial coordinate (R) and angular coordinates (θ and ϕ). The inner and outer boundaries are set at $R = 10$ and $R = 1200$ au, respectively. The grid is nonuniform in the radial direction. The z-axis is aligned with the Sun's rotation axis. The x-axis belongs to the plane formed by the z-axis and the LISM velocity vector, $\boldsymbol{V}_\infty$, and is directed upstream into the LISM. The y-axis completes the right-hand coordinate system. The system of equations is solved using a Godunov-type method of the second order of accuracy in space and time. The numerical fluxes of mass, momentum, energy, and magnetic field through the boundaries of computational cells are obtained by solving a Roe-type MHD Riemann problem solver (Kulikovskii et al. 2000).

3.2. Inner and Outer Boundary Conditions

At the inner boundary, the density and pressure of thermal protons and PUIs are assumed to be spherically symmetric. The velocity is radial, and the heliospheric magnetic field (HMF) is assumed to be a Parker spiral. Since the inner boundary is placed at 10 au while the data are typically available at 1 au, we need to assume something about their behavior in between.

Table 1 summarizes 1 au and outer boundary conditions used in the simulations. The density of thermal protons is assumed to follow an R^{-2} radial dependency for $R \in [1, 10]$ au. This is in agreement with the continuity equation for a steady radial flow with no sources or losses. Thus, $n_{p,th} = 0.01 n_{p,1\ au}$ at 10 au. The temperature of thermal protons at 10 au is specified by $T_{p,th} = T_{p,1\ au} \times 10^{-2\delta+2}$, where we use an effective power index $\delta = 1.42$, which is more suitable for the observed nonadiabatic temperature profile. To obtain the properties of thermal SW at 1 au, we use the OMNI one-day averaged data for the period from 2008 to 2022.[6] This interval is chosen to allow for the comparison of our solutions with the NH observations of thermal SW protons and PUIs between 11 and 47 au measured during the same interval of time. The PUI properties at 10 au are specified on the basis of the NH observations (McComas et al. 2021). In particular, the PUI density and temperature at 10 au are set to 1.5×10^{-3} cm^{-3} and 3.36×10^6 K, respectively.

Table 1
Inner (1 au) and Outer (Unperturbed LISM) Boundary Conditions

Parameters at 1 au	Value
Thermal proton density	9 cm^{-3}
SW speed	420 km s^{-1}
SW temperature	90,000 K
Radial HMF component	39 μG
PUI density at 10 au	1.5×10^{-3} cm^{-3} (McComas et al. 2021)
PUI temperature at 10 au	3.36×10^6 K (McComas et al. 2021)
LISM parameters	**Value**
Proton density	0.054 cm^{-3} (Bzowski et al. 2019)
Flow speed	25.4 km s^{-1} (McComas et al. 2015)
Plasma temperature	7500 K (McComas et al. 2015)
ISMF strength	3.5 μG (Zirnstein et al. 2016)
Neutral H density	0.2 cm^{-3} (Swaczyna et al. 2021)
Velocity direction (HAE-J2000)	(255.°7, 5.°1) (McComas et al. 2015)
ISMF (HAE-J2000)	(224.°46, 36.°61) (Zirnstein et al. 2016)

The choice of inner and outer boundary conditions in the unperturbed LISM is in agreement with currently accepted values. For example, the ISMF strength is chosen to be 3.5 μG, as in Zhang et al. (2020), where this choice was fit to the observed anisotropy of TeV Galactic cosmic rays. The ISMF direction corresponding to this strength is taken from Zirnstein et al. (2016). We adopt the H density suggested by Swaczyna et al. (2021). As the LISM velocity is not necessarily superfast magnetosonic over the entire (spherical) outer boundary, we follow the algorithm proposed in Pogorelov & Semenov (1997) to determine the boundary fluxes (see also Kulikovskii et al. 2000).

4. Treatment of PUIs across the Termination Shock

The PUI behavior near shocks is associated with kinetic processes, which cannot be described in the MHD statement of the problem. It would be suitable to solve the kinetic equations to describe the PUI behavior across the TS. However, this is practically impossible for the problem of the considered space scale. Zank et al. (2010a) proposed a theoretical approach to obtain temperature partition among different types of ions behind one specific point at the TS, which was further used, with slight variations, over the whole TS and throughout the

[6] The values are derived from the OMNI data set, which can be accessed at https://cdaweb.gsfc.nasa.gov/ in the period 2008–2022. The average density from daily averaged data is 6.0 ± 3 cm^{-3}, where the error is the standard deviation of one-day resolution data. For the radial velocity component, proton temperature, and magnetic field magnitude, the values are 410 ± 86 km s^{-1}, $73{,}000 \pm 51{,}400$ K, and 5 ± 1.9 nT, respectively.

IHS in several earlier works (Zirnstein et al. 2017; Heerikhuisen et al. 2019; Shrestha et al. 2020). The energy partition was used to obtain the PUI properties from the plasma mixture instead of solving the equations describing the PUI behavior self-consistently. Recently, Kornbleuth et al. (2023) have used the hybrid simulations of Giacalone et al. (2021) and the theoretical analysis of Wang et al. (2023) to investigate the effect of diffusive shock acceleration on the PUI transmission through the TS in the framework of a global model, which did not include PUIs separately. In addition, rather strong assumptions were made to extrapolate or deduce the properties of PUIs across the entire TS surface and the IHS, with the purpose of fitting the IBEX and Cassini INCA measurements of ENA fluxes in the energy range up to 40 keV.

Pogorelov et al. (2016) solved Equations (1)–(9) self-consistently, but implemented another, simpler approach to determine the PUI properties behind the TS. To address the problem of PUIs crossing the TS in a more comprehensive manner, we now use hybrid simulations (Gedalin et al. 2023) to relate the PUI properties behind the TS to those ahead of it. As typical for hybrid simulations, they treat ions using a kinetic formalism, while electrons are treated as a neutralizing negatively ionized fluid. Thus, the simulations self-consistently describe energization of PUIs and thermal protons at the shock front and a subsequent isotropization of initially highly anisotropic PUIs in the downstream region. The relations derived earlier from test-particle analyses, e.g., by Gedalin et al. (2021b), can only determine the PUI properties in the gyrotropic post-shock region.

The process of isotropization occurs sometimes over distances as large as a few hundred inertial lengths (d_i = 5000 km) of thermal SW protons (Gedalin et al. 2023) and involves self-consistent interactions of ions with plasma instabilities, which are reasonably well described with a hybrid approach. It is worth noting that different species *viz.* PUIs, thermal protons, and electrons, tend to become isotropic over different distances from the shock. The hybrid simulations we use to describe the shock transition have computational boxes extending to more than several hundred ion inertial lengths where the degree of anisotropy remains below 2%. It should be noted that this length is much smaller than the numerical grid size at the TS used in our global simulation (∼1.5 au).

The idea of the new approach is to ignore the solution of Equation (9) for PUI pressure obtained immediately behind the shock, but instead to substitute it with $p_{\rm PUI}$ derived from the hybrid simulations based on the local shock parameters, e.g., the shock speed and normal vector, which are obtained using the MHD solution for the plasma mixture. Hereinafter, we use the superscripts "u" and "d" to indicate quantities in front of the shock (upstream) and behind it (downstream).

Because the PUI pressure and temperature that occur in Equation (9) are scalars, we introduce an isotropic temperature (e.g., see Gedalin et al. 2021b),

$$T^{\rm d}_{\rm iso,PUI} = \left(\frac{2}{3} + \frac{1}{3{\rm A}}\right) T^{\rm d}_{\perp,{\rm PUI}}, \tag{12}$$

where ${\rm A} = T^{\rm d}_{\perp,{\rm PUI}}/T^{\rm d}_{\parallel,{\rm PUI}}$ is the anisotropy index, and $T^{\rm d}_{\parallel,{\rm PUI}}$ and $T^{\rm d}_{\perp,{\rm PUI}}$ are the downstream parallel and perpendicular temperatures of PUIs. As mentioned earlier, in the hybrid solution we select the downstream point in the nearly isotropic region where $A \in [0.99, 1.1]$. The downstream PUI pressure is $p^{\rm d}_{\rm PUI} = n^{\rm d}_{\rm PUI} k_{\rm B} T^{\rm d}_{\rm iso,PUI}$, where $n^{\rm d}_{\rm PUI}$ is the downstream PUI density in our global simulations. Because we assume that all charged species are comoving, continuity requires that the ratio of PUI densities across the shock should be equal to such a ratio available from the MHD equations for the mixture.

A series of 2D hybrid simulations have been conducted to cover the possible range of upstream plasma parameters: the normal Alfvén Mach number ($M_{\rm A} = u_{\rm n}/V_{\rm A}$); shock angle $\theta_{\rm Bn} = (180/\pi)\cos^{-1}(\boldsymbol{b}\cdot\boldsymbol{n})$, where $\boldsymbol{b} = \boldsymbol{B}/B$ is the unit magnetic field vector and $\boldsymbol{n}$ is the shock normal; plasma beta $\beta = p/p_{\rm mag}$; and the ratio of PUI density to total proton density ($\xi = n_{\rm PUI}/n$) upstream of the TS. Here, $u_{\rm n} = \boldsymbol{u}\cdot\boldsymbol{n}$, $V_{\rm A} = B/\sqrt{4\pi\rho}$, p, and $p_{\rm mag}$ are the normal component of bulk velocity, Alfvén speed, and thermal and magnetic pressures, respectively. The hybrid simulation model is the same as used in Gedalin et al. (2023). The results of hybrid simulations for $T^{\rm d}_{\rm iso,PUI}/T^{\rm u}_{\rm PUI}$ created a cloud of points depending on the shock properties, which were further approximated by surfaces in parametric space. The covered range of shock parameters in the hybrid simulations is approximately the following: $M_{\rm A} \in [7, 25]$, $\beta \in [10, 50]$, $\theta_{\rm Bn} \in [70°, 87°]$, and $\xi \in [0.2, 0.4]$. This range covers the latitudes within ±80° sufficiently well in our global simulation. For latitudes $|\delta| \gtrsim 80°$, the upstream Mach number and plasma beta increase significantly ($M_{\rm A} \gtrsim 50$ and $\beta \gtrsim 70$), due to the decrease in the magnetic field strength toward the poles. We note that this occurs because the magnetic field in the supersonic SW in our steady-state solution essentially follows the Parker model. In reality, Ulysses observations showed that, owing to large-amplitude fluctuations, the magnetic field exceeded the Parker values in the polar regions (Balogh et al. 1995). This issue will be discussed in more detail later.

In Figure 1, we present the distributions of $T^{\rm d}_{\rm iso,PUI}/T^{\rm u}_{\rm PUI}$ and $p^{\rm d}_{\rm PUI}/p^{\rm u}_{\rm PUI}$ obtained from our hybrid simulations as function of $M_{\rm A}$ and $\theta_{\rm Bn}$ for $\xi = 0.2$, 0.3, and 0.4. In panel (a), each discrete point corresponds to one hybrid simulation, while the continuous surfaces show their functional form obtained through a third-order polynomial interpolation ensuring root mean square (rms) errors below 0.07. Panels (b) and (c) show the temperature and pressure ratio, respectively, as a function of $M_{\rm A}$ for fixed values of $\theta_{\rm Bn}$.

An interesting feature that follows from the results presented in Figure 1 is the presence of a certain saturation of the temperature ratio dependence on the Alfvénic Mach numbers for fixed values of ξ and $\theta_{\rm Bn}$. We take advantage of this feature to extrapolate the hybrid solutions to high $M_{\rm A}$ occurring in the polar regions. The second important observation is that the shock compression ratio is different for every point belonging to each approximation surface shown in Figure 1. In the simulations presented in Figure 1, the normalized upstream PUI temperature ($k_B T^{\rm u}_{\rm PUI}/(m_{\rm p} U^2)$, where U is the upstream speed and m_p is the mass of the proton) ranges from 0.14 to 0.16. The beta of thermal protons ($\beta_{\rm p,th} = p_{\rm p,th}/p_{\rm mag}$) is equal to 0.1. In principle, the upstream temperatures in the global model can deviate from the above values. We emphasize that the parameterization of our hybrid simulation results in terms of $M_{\rm A}$, $\theta_{\rm Bn}$, and ξ is insufficient to uniquely describe the shock because ξ refers only to PUI properties. However, we found that the temperature ratio $T^{\rm d}_{\rm iso,PUI}/T^{\rm u}_{\rm PUI}$ can actually be expressed as a function of three parameters only, e.g., the compression ratio ($\rho^{\rm d}/\rho^{\rm u}$), the upstream Alfvénic Mach

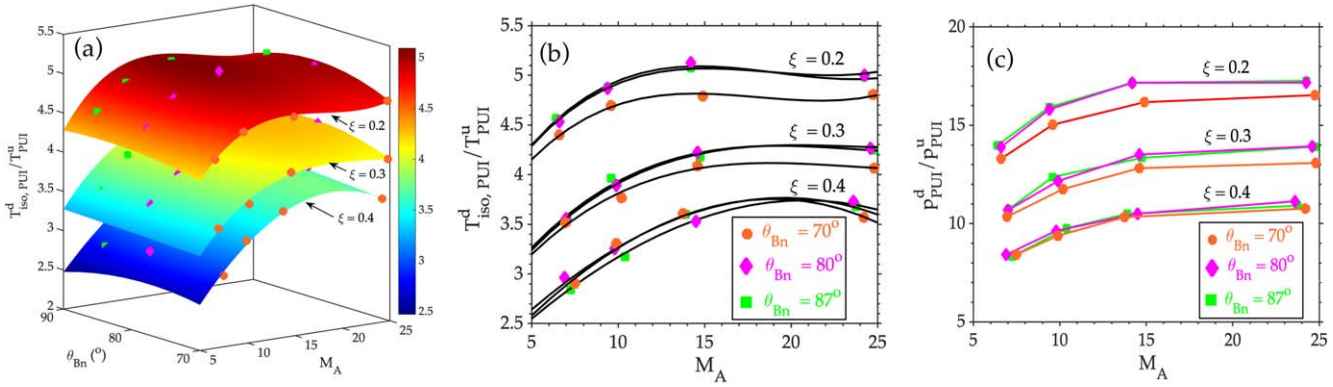

Figure 1. Distributions of the downstream to upstream PUI temperature and pressure ratios obtained from the hybrid simulations in the parameter space of M_A, θ_{Bn}, and ξ. Panel (a): dependence of $T^d_{iso,PUI}/T^u_{PUI}$ on M_A and θ_{Bn} for $\xi = 0.2$, 0.3, and 0.4 is shown with symbols, while the best fits obtained with polynomial functions for each ξ are shown with color-coded surfaces. Panel (b): one-dimensional dependencies of the temperature ratios on M_A for chosen ξ and θ_{Bn}; the black lines show the best-fit analytic functions. Panel (c): the same as in panel (b), but for the pressure ratios.

number, and the shock angle, as follows:

$$T^d_{iso,PUI}/T^u_{PUI} \approx f(M_A, \theta_{Bn}, \rho^d/\rho^u), \quad (13)$$

where f is a function of the three variables. The approximate equality sign is used in Equation (13) because the details of the shock structure may depend on other factors (e.g., the shape of the upstream PUI distribution function, presence of turbulence, etc.). The boundary conditions for PUIs at the TS in the form of Equation (13) cannot be directly used in the global model, even though the compression ratios are always available from the global simulation of the plasma mixture. This is because shock smearing intrinsic to shock-capturing methods makes the determination of this parameter uncertain, as it depends on the selection of the upstream and downstream computational cells at each shock point. Because the dependency of $T^d_{iso,PUI}/T^u_{PUI}$ on the upstream-to-downstream density ratio is strong, an improper selection of the compression ratio can result in large errors in the downstream PUI temperature and lead to unphysical fluctuations in the PUI distribution in the IHS. It is therefore desirable to find a parameterization of the $T^d_{iso,PUI}/T^u_{PUI}$ dependence on the upstream parameters only—in other words, to recalibrate the results of hybrid simulations.

According to the Rankine–Hugoniot relations applied to the plasma mixture, ρ^d/ρ^u can be uniquely substituted with the upstream plasma beta. Hence, the PUI temperature ratio can be expressed as

$$T^d_{iso,PUI}/T^u_{PUI} \approx g(M_A, \theta_{Bn}, \beta). \quad (14)$$

Here, g represents a function of the upstream quantities, i.e., M_A, θ_{Bn}, and β. This is the parameterization that we used to express the shock boundary conditions for PUIs in our global simulations. In Figure 2, we show the distributions of $T^d_{iso,PUI}/T^u_{PUI}$ in the form of Equation (14) derived from the hybrid simulations. In panels (a), (b), and (c), the 2D distributions of $T^d_{iso,PUI}/T^u_{PUI}$ are shown as functions of M_A and β for $\theta_{Bn} = 70°$, 80°, and 87°, respectively (the color plots show the piecewise linearly interpolated values). The black points show the values of M_A and β upstream of the TS occurring in our global simulation. In panels (d) and (e), the function (14) is plotted for constant values of β and M_A. It can be seen that $T^d_{iso,PUI}/T^u_{PUI}$ strongly depends on M_A and β with a weaker dependence on shock angle θ_{Bn} (in the considered range).

As mentioned previously, the upstream M_A and β in our simulations can be very large in the polar regions, due to the small magnetic field strength. Although this may not be the case in a real, data-driven system, we still need to cover all TS points in our solutions. This presents a challenge, as it is not trivial to extrapolate the results in the form of Equation (14) to large M_A and β, because of the strong dependence of M_A and β on each other. We therefore take advantage of the above-mentioned saturation in the dependence of our results on the Mach number (see Figure 1) and the weak dependence of the compression on M_A ($\gg$1). We extended function (13) assuming that $T^d_{iso,PUI}/T^u_{PUI}$ stops changing for $M_A > 25$, as suggested by Figure 1, and remapped the results to obtain them in the form of Equation (14). The outcome is shown in panel (f) of Figure 2. The results for $T^d_{iso,PUI}/T^u_{PUI} = g(M_A, \theta_{Bn}, \beta)$ are stored in a high-resolution lookup table, which is used when running the global code.

5. Results

5.1. Distributions of Quantities in the Supersonic SW and Comparison with the NH and V2 Data

Let us first look at our solutions in the supersonic SW before the TS and compare them with NH and V2 observations. The NH plasma instrument Solar Wind Around Pluto (SWAP) measures the properties of both thermal protons and PUIs (McComas et al. 2008; Elliott et al. 2016). Currently, this is the only spacecraft that provides such data beyond Mars. McComas et al. (2021) describe SWAP data for heliocentric distances from 11 to 47 au measured in the time interval between 2008 and 2020. Figure 3 illustrates a comparison of our model results with the observations made by NH and V2 in the supersonic SW. We use daily averages of NH data from 2008 to 2020 (11–47 au) and monthly averages of V2 data measured from 1986 to 2006 (10–80 au). Because NH has no magnetometer, we only compare the model magnetic field strength with the V2 data.

The overall agreement between the simulations and observational data is reasonable. Admittedly, even the radial trend in the temperature distribution of thermal protons is also reproduced with our simplified approach to calculating S_w. Because we modify the source term only in Equation (9) and

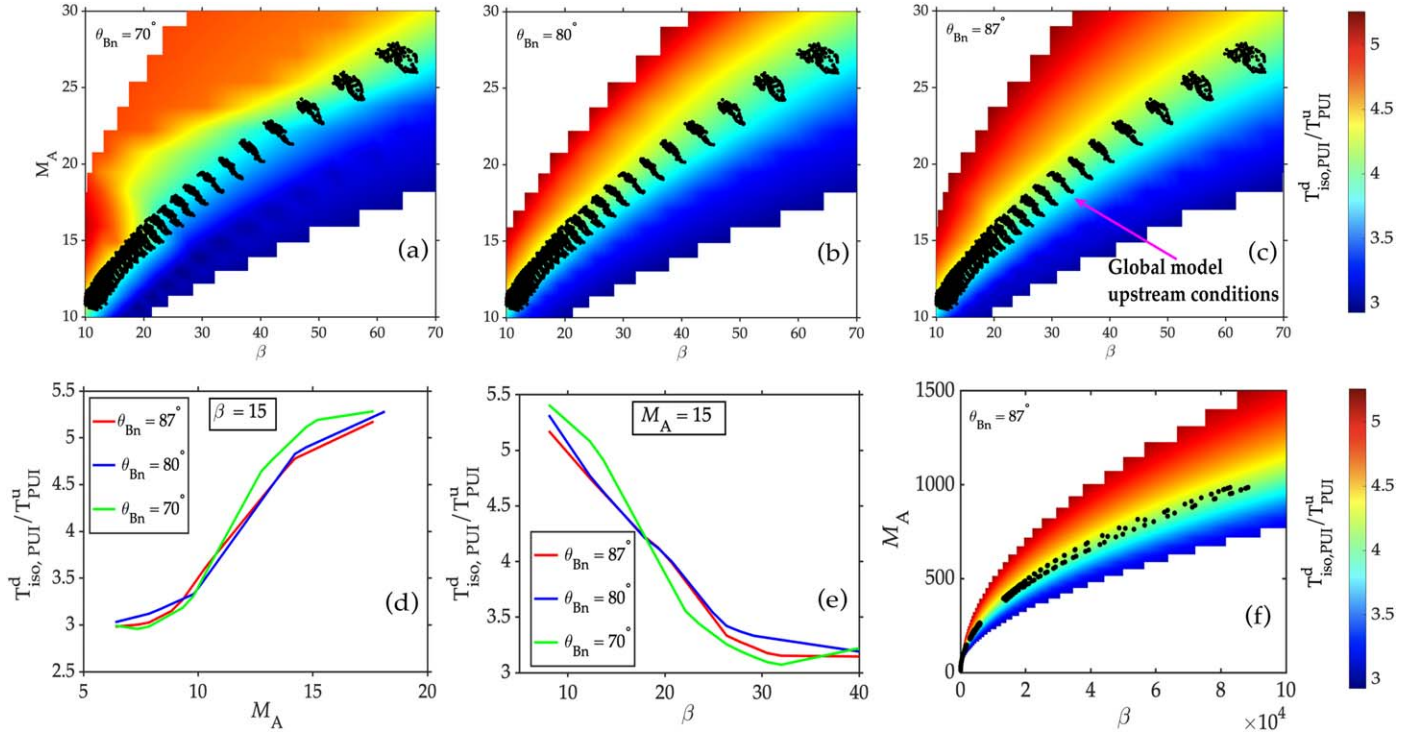

Figure 2. Distributions of $T^{d}_{iso,PUI}/T^{u}_{PUI}$ obtained from the hybrid simulations in the parameter space of M_A, θ_{Bn}, and β. The top panels show 2D distributions for three different shock angles. The black dots in the figure represent the values of M_A and β in our global model. One-dimensional extractions of the dependency of $T^{d}_{iso,PUI}/T^{u}_{PUI}$ on the Mach number and plasma beta are shown in panels (d) and (e). Panel (f) shows the distributions of $T^{d}_{iso,PUI}/T^{u}_{PUI}$ in the extended range of parameters $M_A \in [1, 1500]$ and $\beta \in [1, 1 \times 10^5]$.

keep the source terms in Equations (1)–(3) unchanged, the temperature of the thermal SW increases, reaching ∼20,000 K in front of the TS in our simulation, which agrees with the observations made by V2 (Richardson et al. 2008).

Interestingly, the average density of thermal protons measured by NH is consistently higher than that in V2 observations. As a consequence, the average bulk speed is consistently lower. This may be due to the difference in the time intervals covered by the measurements. Elliott et al. (2019) showed that the density distribution of thermal protons in the NH observations exhibits a radial exponent of −1.83. On the other hand, the radial exponent is equal to −1.93 at V2 (Richardson et al. 1996). Being stationary, however, our model cannot address this issue. Time-dependent simulations similar to those in Kim et al. (2016, 2018) should be performed for this purpose.

The radial exponent in the density distribution of thermal protons in our steady-state simulation is ∼−2.0 up to 80 au, which corresponds to a purely spherical expansion. The density of all protons (thermal and PUIs), however, falls as $R^{-1.93}$ for $R \in [10, 45]$ au and $R^{-1.84}$ for $R \in [45, 80]$ au, in agreement with the SW slowdown due to the PUI production. It is worth noting that we needed to increase the density of thermal protons at 1 au to 9 cm^{-3} in order to make the simulations agree with the NH density distributions. While the increase is ∼20% of the average density at 1 au in the interval 2012–2021 (OMNI data), it still remains within the standard deviation of the measurements.

5.2. Effects of the TS Boundary Conditions on the Global SW–LISM Interaction

Let us examine the impact of our newly developed relations for PUIs crossing the TS on the overall pattern of the SW–LISM interaction. We compare two models hereinafter called `Model 1` and `Model 2`. In `Model 1`, the simulations do not involve any specific additional treatment of PUIs across the shock, i.e., Equation (9) is solved in its current form throughout the simulation domain and numerical approximation of space derivatives occurring in this equation across the TS is allowed. In `Model 2`, our new b.c.s for PUIs are used at the TS while solving Equation (9).

In panels (a) and (b) of Figure 4, we show the distributions of PUI pressure in the meridional (xz) plane for Models 1 and 2. The meridional plane is defined by the Sun's rotation axis (the z-axis in our simulation) and the velocity vector in the uniform, unperturbed LISM. The HP location is indicated with the black dashed and solid lines for `Models 1` and `2`, respectively. The distributions of the PUI pressure in the equatorial plane are shown in Figure 5 (panels (a) and (b)). It can be seen that we obtain higher PUI pressure immediately downstream of the TS for all radial directions, in both meridional and equatorial planes, in `Model 2` as compared to `Model 1`.

Panels (c) and (d) of Figure 4 show the temperature distributions for the plasma in the meridional plane for both Models `1` and `2`. The same distributions in the equatorial plane are shown in Figures 5(c) and (d). We find that the plasma temperature in the IHS becomes lower when the PUI b.c.s are used. This leads to a reduction of the IHS width, as seen in Figures 4(d) and 5(d), where the HP locations in both models are shown for comparison. The IHS width along the x-axis in the upwind direction becomes smaller by ∼8–10 au in `Model 2`. Such a reduction is even more pronounced on the downwind side.

In Figures 6(a)–(e), we present the distributions of θ_{Bn}, density compression, PUI-to-proton density ratio, and downstream PUI-to-proton temperature and pressure ratios (T^{d}_{PUI}/T^{d}_{p}

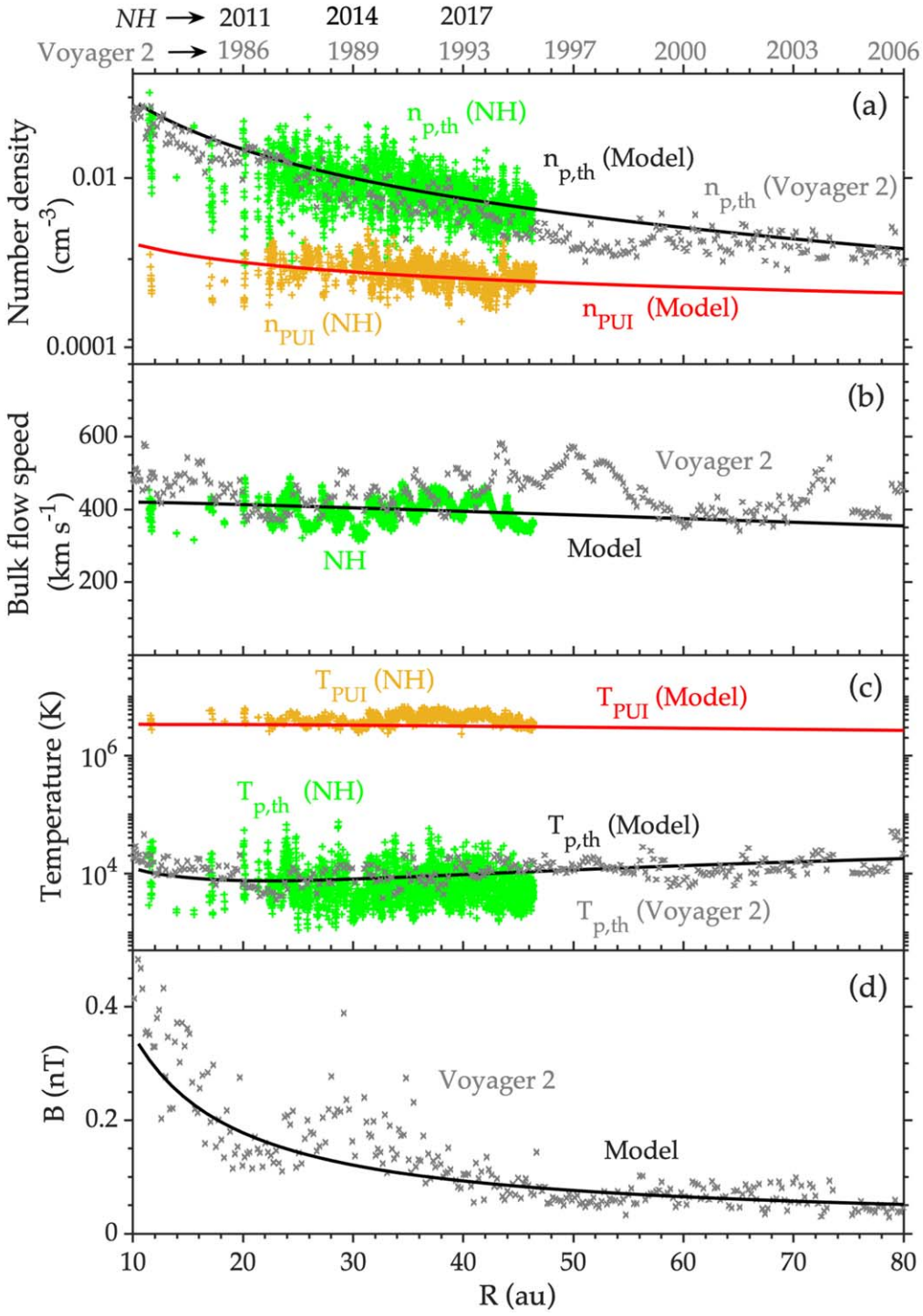

Figure 3. Comparison of solutions obtained from our simulation with the NH and V2 observations in the supersonic SW for $R \in [10, 80]$ au. The black solid lines of panels (a) and (c) show the distributions of number density and temperature obtained from the simulation for thermal protons. The number density of the PUIs and their temperature obtained from the simulation are shown in red solid lines in panels (a) and (c). The green and orange points represent the daily averages of NH data for thermal proton and PUI quantities, respectively, for $R \in [11, 47]$ au. Panels (b) and (d) show the bulk flow speed and the magnetic field strength, respectively. The monthly averaged V2 data are shown with gray cross symbols.

and $p^{\rm d}_{\rm PUI}/p^{\rm d}_{\rm p}$) obtained with `Model 2` over the TS. In panel (f), we compare our PUI temperature behind the TS with the one obtained with the model of Shrestha et al. (2020, henceforth SZH20; see also Heerikhuisen et al. 2019). In SZH20, the energy partition between PUIs and thermal protons downstream of the TS is based on Zank et al. (2010a) and includes thermal SW ions as well as reflected and transmitted PUIs. According to that model, the PUI temperature downstream of TS can be then written as

$$T_{\rm PUI,SZH10} = T^*(\Gamma_{\rm tran}(1-\beta_{\rm ref}) + \Gamma_{\rm ref}\beta_{\rm ref}), \quad (15)$$

where T^* is obtained from the following expression:

$$[(2-\xi)\Gamma_{\rm p,th} + \Gamma_{\rm tran}\xi(1-\beta_{\rm ref}) + \Gamma_{\rm ref}\xi\beta_{\rm ref}]T^* = 2T^{\rm d}. \quad (16)$$

Here, $\beta_{\rm ref} = n^{\rm ref}_{\rm PUI}/n_{\rm PUI}$ is the fraction of reflected PUI density and $T^{\rm d}$ is the downstream plasma temperature. In addition, $n^{\rm ref}_{\rm PUI}$

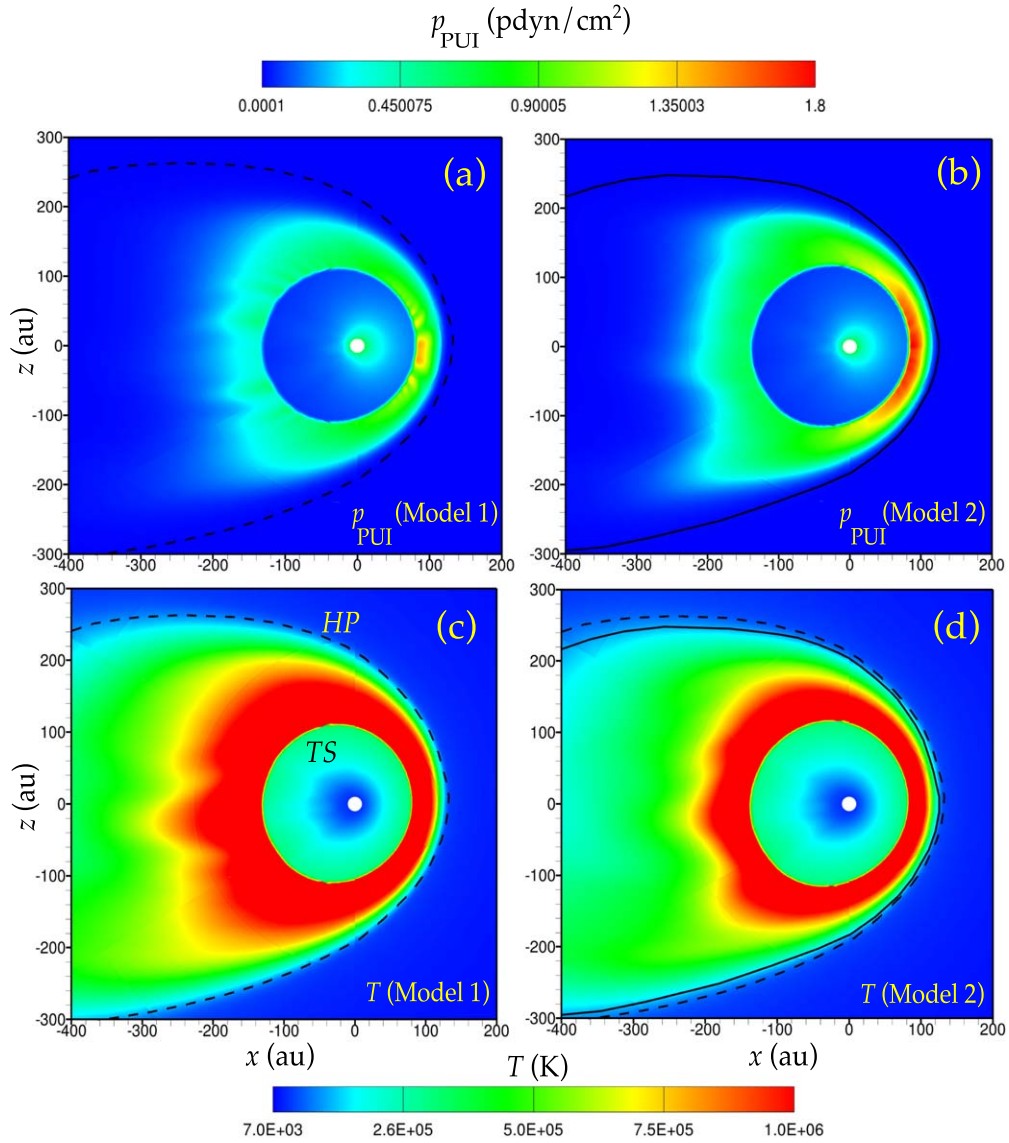

Figure 4. Distributions of PUI pressure (top panels) and plasma temperature (bottom panels) in the meridional plane for `Model 1` (left panels) and `Model 2` (right panels). The HP positions are shown with the black dashed and solid lines for `Models 1` and `2`, respectively.

is the density of reflected PUIs, T^* represents a modified temperature of all protons, and $\Gamma_{p,th} = T_{p,th}/T^*$, $\Gamma_{ref} = T^{ref}_{PUI}/T^*$, and $\Gamma_{tran} = T^{tran}_{PUI}/T^*$ are the temperature ratios. The quantities $\Gamma_{p,th}$, Γ^{tran}_{PUI}, Γ^{ref}_{PUI}, and β^{ref}_{PUI} are typically assumed constant over the entire TS in Zirnstein et al. (2017), Heerikhuisen et al. (2019), and Shrestha et al. (2020). That is, the downstream temperature of PUIs is calculated solely on the basis of the downstream plasma temperature.

In Figure 6(f), we show the ratio of the downstream PUI temperature obtained from `Model 2` to that obtained using Equations (15)–(16) assuming $\Gamma_{p,th} = 0.06$, $\Gamma_{ref} = 22.6$, $\Gamma_{tran} = 2.9$, and $\beta^{ref}_{PUI} = 0.093$ as in Shrestha et al. (2020). While the pressure ratio $p^d_{PUI}/p^d_p = \xi\, T^d_{PUI}/T^d_p$ is nearly constant over the TS in the aforementioned model, panel (e) shows that it can vary considerably, with changes up to 20% in the present simulation. As compared with SZH20, our model results in higher PUI temperatures (by 7%–8%) at the TS flanks and in the polar regions. These are the regions with the highest PUI-to-proton pressure ratio that correspond to the least perpendicular segments of the TS. The test-particle analysis of Gedalin et al. (2021a) shows that the number of reflected ions rapidly increases with the decrease of θ_{Bn}. As a result, the downstream PUI temperature becomes higher for smaller shock angles. At the same time, our model gives comparably lower temperatures on the upwind and downwind sides of the TS, which is also consistent with the lower temperatures of reflected PUIs (and higher number density) found by Gedalin et al. (2021a), as compared to SZH20. Our results are particularly important for time-dependent simulations, where the TS can have a wider range of shock angles, due to the presence of ripples on the shock surface and solar cycle effects (Pogorelov et al. 2009a, 2012, 2013; Borovikov et al. 2012; Zirnstein et al. 2022).

In Figure 7, we present the linear distributions of the proton density ($n = n_{p,th} + n_{PUI}$), and plasma pressure and temperature along the x-axis from 40 to 400 au for both models. The number density, pressure, and temperature associated with the thermal protons and PUIs are also shown. It can be seen that the distributions of plasma quantities undergo significant changes in `Model 2`. The changes are more pronounced in the IHS and in the outer heliosheath (OHS) than in the

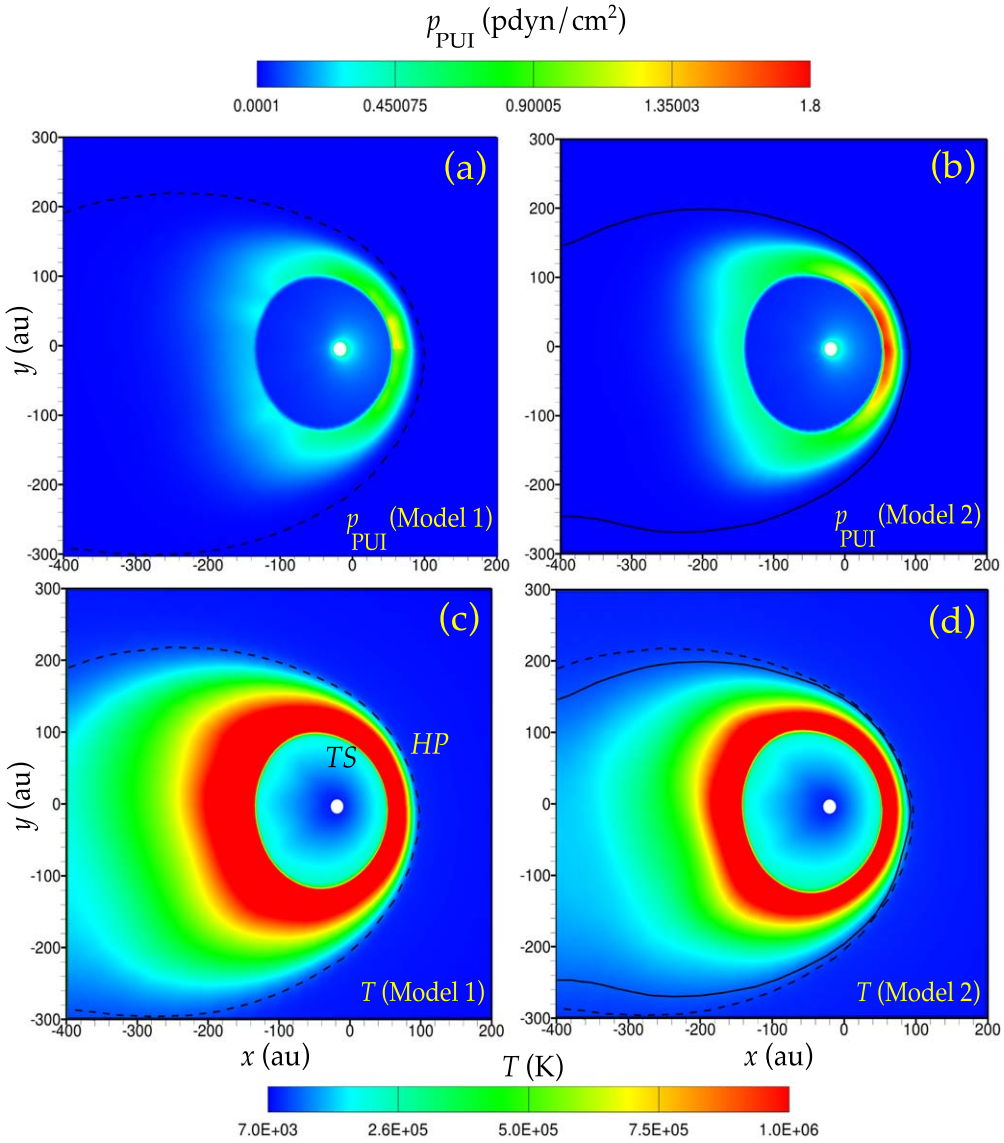

Figure 5. The same as in Figure 4, but in the equatorial plane.

supersonic SW. Notably, the OHS defines an LISM region relatively close to the HP, where the plasma temperature exceeds the unperturbed value by a somewhat arbitrary threshold set to ∼3% (Fraternale et al. 2023).

For better comparison of the solutions obtained in `Model 1` and `2` in the upwind and downwind sides, in Figure 8 we show the distributions of the temperature of the plasma, PUIs, and thermal protons along the x-axis from −400 to 200 au. The PUI temperature appears to be $\gtrsim$60% higher behind the TS when the new shock relations are applied to PUIs. It is of interest, however, that the temperature of the plasma is lower in the IHS, especially near the HP, in `Model 2`. As can be seen, the reduction of plasma temperature is more pronounced in the downwind direction for $x \in [-400 - 200]$ au. This is due to the changes in the charge-exchange sources caused by hotter PUIs and colder thermal protons (see Section 5.3 for a more detailed discussion).

While direct measurements of PUI properties in the IHS are not yet available, our new model appears to be in better agreement with the thermal proton measurements by V2 at the TS. The temperature of thermal protons just behind the TS along the V2 direction becomes ∼180,000 K, which agrees with V2 measurements (Richardson et al. 2008). On the other hand, the thermal proton temperature is overestimated by a factor of ∼6 in `Model 1`, due to the inaccurate energy partition between the thermal and nonthermal ions at the TS crossing.

5.3. Effects of Charge Exchange in the IHS and on the Plasma Temperature

An indirect but significant consequence of the accurate treatment of PUIs across TS is an enhanced cooling of the plasma mixture in the IHS obtained in `Model 2`. This results in the higher (negative) radial gradient of temperature obtained in `Model 2` and consequently in the colder plasma away from the TS, as shown in Figure 8 (red curves).

Let us identify the physical mechanism responsible for the plasma cooling in the IHS. Figure 9 shows the distributions along the x-axis for the rates of change of number density (left panels), pressure (central panels), and temperature (right panels) due to charge exchange. From the top to the bottom, these quantities are shown for the plasma, thermal protons, and PUIs.

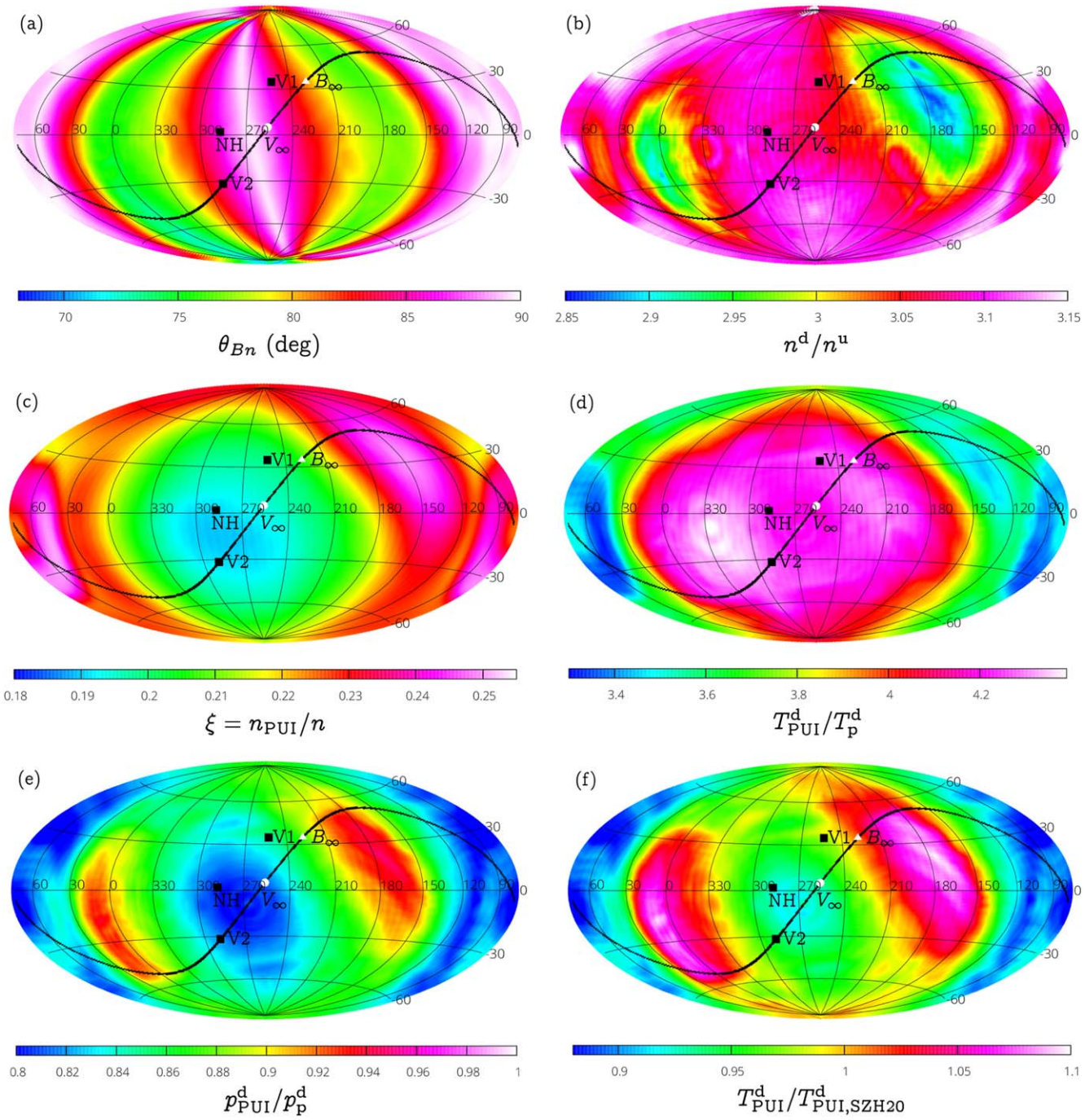

Figure 6. The distributions of the following quantities are shown in projection on the TS surface: (a) upstream shock angle ($\theta_{\rm Bn}$); (b) compression ratio; (c) PUI-to-proton density ratio; (d) downstream PUI-to-proton temperature ratio; (e) downstream PUI-to-proton pressure ratio; and (f) ratio of our PUI temperature to the one obtained with the model of Shrestha et al. (2020). The distributions are presented in the Solar Ecliptic J2000 coordinates centered along the x-axis. The positions of V1 and V2 at the moment of their crossing of the TS, the NH current position, and the projection of the B_∞–V_∞ plane onto the TS surface (solid black line) are also shown. It should also be noted that each panel utilizes distinct ranges for the colorbar.

To avoid confusion, we note that some of the presented source terms (e.g., the one for the temperature) do not occur in Equations (1)–(9) explicitly, but still can be computed from the mass, momentum, and energy source terms using the equation of state and relation (10). The charge-exchange-induced heating rate for the entire plasma can be calculated as

$$S^T \equiv \frac{DT}{Dt}\bigg|_{\rm ch-ex} = \frac{T}{p}(S^p - \frac{p}{\rho}\cancel{S^\rho}),$$

while the one for an individual ion or a neutral atom component s is

$$S^T_s = \frac{T_s}{p_s}\left(S^p_s - \frac{p_s}{\rho_s}S^\rho_s\right),$$

where the last term vanishes for the ion mixture because no new particles are created during charge exchange. This is seen from panel (a) in this figure, where $S^n = 0$.

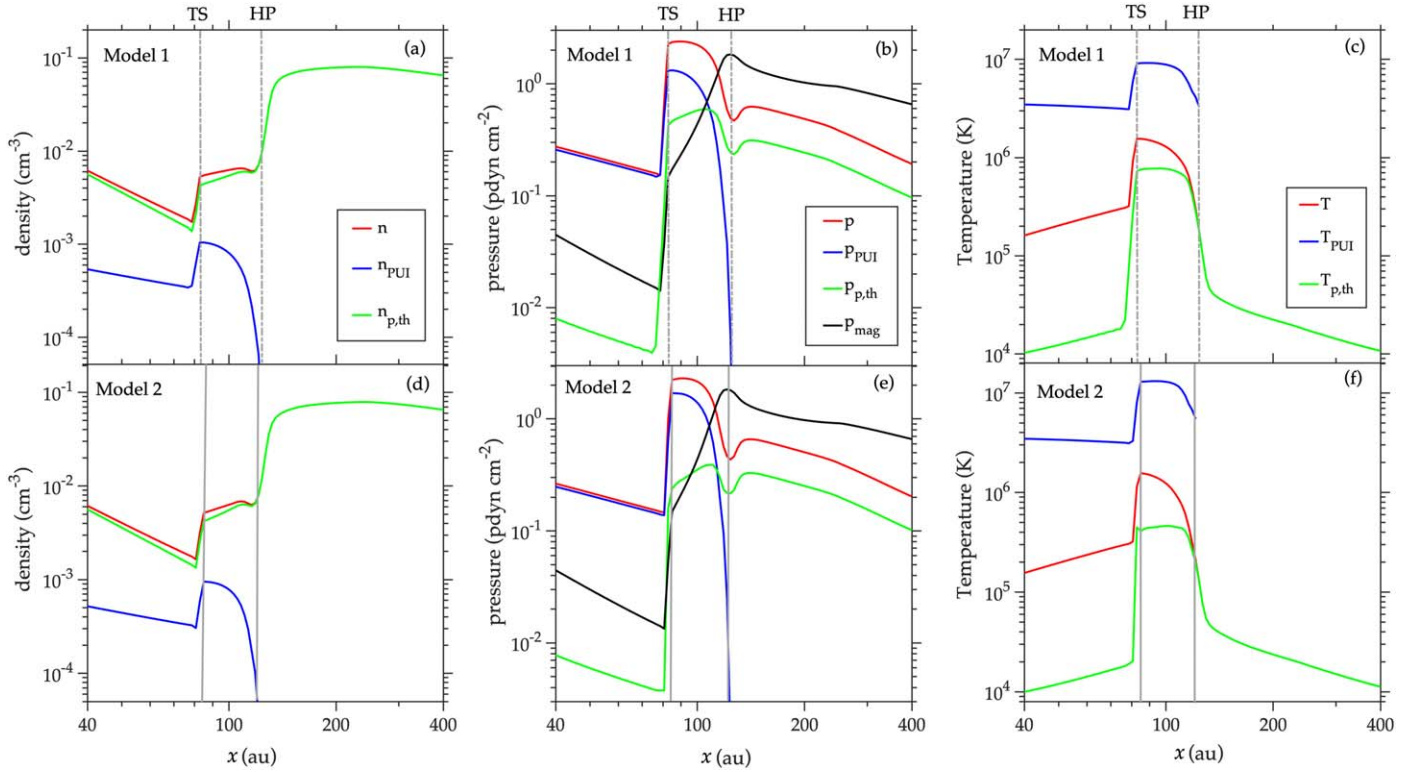

Figure 7. Distributions of the plasma density, pressure, and temperature along the x-axis from 40 to 400 au for `Model 1` (panels (a)–(c)) and `Model 2` (panels (d)–(f)). The TS and HP are shown with dashed and solid gray vertical lines for `Models 1` and `2`, respectively.

The sources for thermal protons are derived a posteriori:

$$S^{p}_{\rm p,th} = S^{p} - S^{p}_{\rm PUI}, \quad S^{\rho}_{\rm p,th} = -S^{\rho}_{\rm PUI}.$$

We recall here that Equations (8) and (9) describe the density and pressure of PUIs born in the supersonic SW and propagating through the heliosphere. As mentioned earlier in Section 2, PUIs that experience charge exchange in the IHS are only lost, i.e., $S^{\rho}_{\rm PUI} \leqslant 0$.

Since `Model 2` gives us higher PUI and lower SW temperatures in the IHS, PUIs have a higher probability of charge exchange with the ISN atoms. This probability decreases for the thermal protons, as seen from panels (d) and (g) of Figure 9.

Since PUIs are energetically dominant, the plasma temperature is mostly determined by the PUI temperature. It can be seen that the sources of pressure and temperature due to charge exchange for both plasma and PUIs are negative in the IHS, while their absolute value is greater in `Model 2`. This clearly indicates that the rates of cooling for the plasma and PUIs are higher in `Model 2`. This can be understood by considering the cooling rates due to charge exchange for thermal protons and PUIs separately. As compared to `Model 1`, the cooling rate for thermal protons in `Model 2` decreases, actually becoming a heating rate downstream of the TS (see panel (i)). In contrast, hotter PUIs in `Model 2` experience additional cooling, and because they are energetically dominant, the plasma experiences additional cooling as well.

As shown by DeStefano & Heerikhuisen (2017) and Heerikhuisen et al. (2019), the energy transfer due to charge exchange associated with the energetic tails typical to Lorentzian distribution functions (with small kappa) may be reduced, because of the resonant nature of this process, which is characterized by a strong reduction of the cross section at energies above 10 keV. However, it is important to note that the actual shape of the PUI distribution in the IHS is still subject to debate. In principle, several PUI populations may exist, and their distribution functions evolve with distance from the TS (Malama et al. 2006).

5.4. Distributions of the Neutral Atoms in `Model 1` and `2`

In this section, we discuss how the application of `Model 2` affects the flow of different populations of neutral H atoms. The top panels of Figure 10 show that the density distributions of $H_{(1)}$ atoms in both models is practically the same. However, there is a notable change in their temperature and pressure, which are enhanced by about 10%–15% and 5%–10%, respectively. The most remarkable changes are seen in the distributions of $H_{(2)}$, as shown in the middle panels of Figure 10. These population 2 atoms are born in the IHS from the following charge-exchange reactions:

$$H^{+}_{\rm th} + H_{(j)} \rightarrow H_{(2)} + H^{+}_{\rm th}, j = 1, 2, 3, \quad (17)$$

$$H^{+}_{\rm PUI} + H_{(j)} \rightarrow H_{(2)} + H^{+}_{\rm th}, j = 1, 2, 3, \quad (18)$$

where $H^{+}_{\rm th}$ indicates a thermal proton. In `Model 2`, the $H_{(2)}$ density in the IHS is lower than in `Model 1` by ∼30%, while their pressure and temperature are higher by ∼30% and ∼60%, respectively. This decrease in density can be understood by noticing that the probability of process (17) in `Model 2` is lower than in `Model 1` because thermal protons are colder, as discussed in Section 5.3. The opposite is true for process (18), due to hotter PUIs. Because the thermal protons dominate the ion number density in the IHS, process (17) is more frequent than process (18), which explains the observed net decrease in the $H_{(2)}$ density.

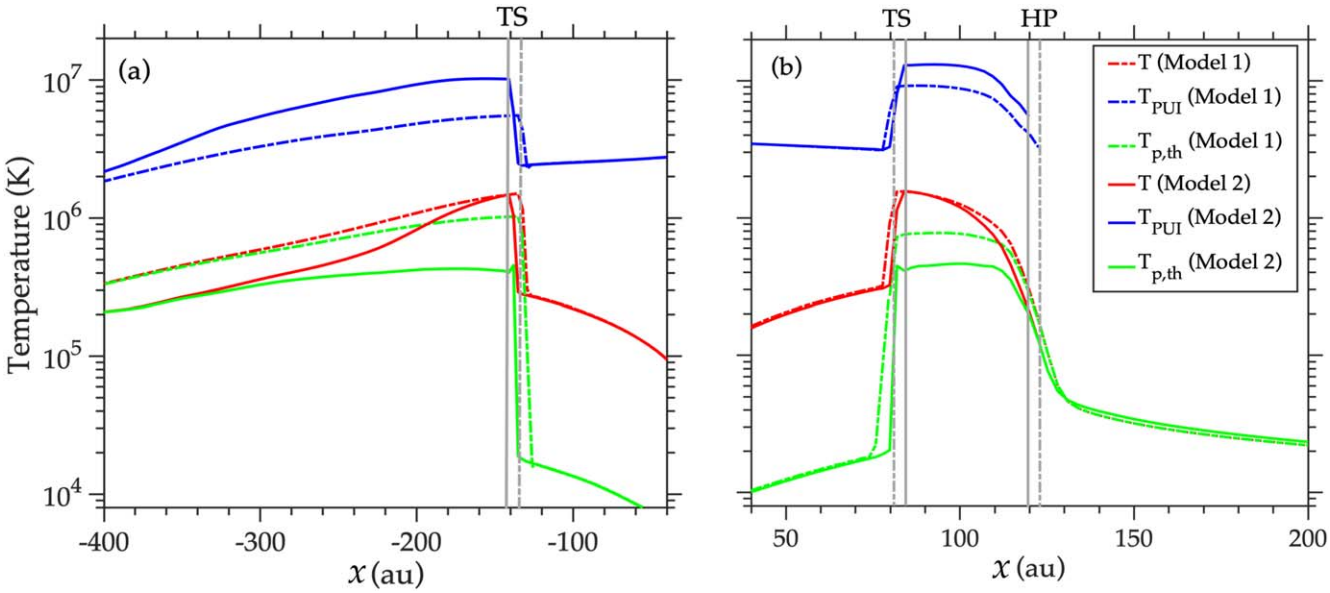

Figure 8. Distributions of the temperature of the plasma (T), PUI ($T_{\rm PUI}$), and thermal proton ($T_{\rm p,th}$) in `Model 1` (dashed lines) and `Model 2` (solid lines) along the x-axis. Panel (a) shows the distributions on the downwind side from $x = -400$ to -40 au. Panel (b) shows the distributions on the upwind side from $x = 40$ to 200 au.

In contrast, the increase in the $H_{(2)}$ pressure and temperature is due to the increase in the probability of process (18) and PUIs being energetically dominant. Once $H_{(2)}$ are created in the IHS, they move to the other regions, where similar changes in their properties are observed. As shown in the bottom panels of Figure 10, there are no significant changes in the properties of $H_{(3)}$.

The changes that the application of `Model 2` imposes on the neutral atom flow can be understood by considering the charge-exchange source terms that appear in Equations (5)–(7). They are associated with the rate of change of density, pressure, and temperature of different populations of neutral H atoms (see Figure 11).

As seen from Figure 11 (panels (b) and (c)), there are no significant changes in the pressure and temperature source terms for $H_{(1)}$ in the IHS, but the corresponding changes in the pressure and temperature source terms in the OHS are noticeable (see radial distances from 130 to 140 au). The higher pressure and temperature source terms for $H_{(1)}$ can be attributed to the enhancements in $H_{(2)}$ pressure and temperature in the OHS. This increase in $S^{p}_{H_{(1)}}$ and $S^{T}_{H_{(1)}}$ can be attributed to the charge-exchange process as follows. In `Model 2`, hotter $H_{(2)}$ eventually propagates into the OHS filled with the LISM. When they undergo charge exchange with the LISM protons, hotter thermal ions are created. We indeed observe higher LISM proton temperature in Model 2 (see Figure 8(b)). When these hotter ions experience further charge exchange with ISN in the LISM, they produce hotter $H_{(1)}$ atoms. These atoms can move throughout the SW–LISM interaction region, which results in higher $H_{(1)}$ pressure and temperature, as seen from panels (b) and (c) in Figure 10.

The middle panel of Figure 11 shows that the density source term for $H_{(2)}$ ($S^{n}_{H_{(2)}}$) is smaller in the IHS if `Model 2` is used. In contrast to the $H_{(2)}$ density source term, the pressure and temperature source terms are larger (see Figures 11(d) and (e)). As a result, the pressure and temperature of $H_{(2)}$ are higher, while the density of $H_{(2)}$ becomes lower.

It is clear from the bottom panels of Figure 11 that no significant differences exist in the $H_{(3)}$ density, pressure, and temperature source terms for both models. Due to the low density of $H_{(3)}$ in the IHS, as compared with the densities of $H_{(2)}$ and $H_{(1)}$, the probability of charge exchange between $H_{(3)}$ and protons is much lower than the ones for $H_{(2)}$ and $H_{(1)}$. As a result, the differences in the thermal and PUI properties in the IHS do not significantly affect the source terms and the flow of $H_{(3)}$ atoms in the heliosphere (as seen in Figure 10).

5.5. Implications for ENA Properties

The changes in flow parameters of PUIs and $H_{(2)}$ make it possible to check whether the new model may yield higher ENA fluxes. It is understood that the quantification of ENA production in a given energy range requires the velocity distribution functions for both PUIs and neutrals. Therefore, at this point we do not attempt to synthesize a comprehensive description of ENA production and reproduce the IBEX measurements. However, it is possible to investigate the behavior of energy-integrated ENA fluxes and their differences in `Models 1` and `2`. This analysis allows us to address potential implications of the new model for the IBEX measurements.

The charge-exchange process that is responsible for the ENA production from PUIs in the IHS can be written as

$$H^{+}_{\rm PUI} + H_{(j)} \rightarrow H_{\rm ENA} + H^{+}_{\rm th}, \quad (j = 1, 2, 3).$$

The density, momentum, and energy source terms for ENAs are equal—but opposite in sign—to the corresponding source terms for PUIs in IHS. In Figure 9(d), it is shown that the density source terms for PUIs ($S^{n}_{\rm PUI}$) in the IHS in `Model 2` is 20% higher (in absolute value). This indicates that the ENA production rate in `Model 2` can be ∼20% higher than in `Model 1`. The PUI energy source term $S^{\rm E}_{\rm PUI}$ is computed from Equation (10). In Figure 12, we show the radial distribution of $S^{\rm E}_{\rm PUI}$ along the x-axis from 70 to 140 au in `Models 1` (red dots) and `2` (blue plus symbols). It can be seen that $S^{\rm E}_{\rm PUI}$ in IHS is less by 50% in `Model 2` as compared to `Model 1`, indicating that more energetic PUIs are generated in the IHS in the new model. Therefore, more energetic ENAs are expected to be produced

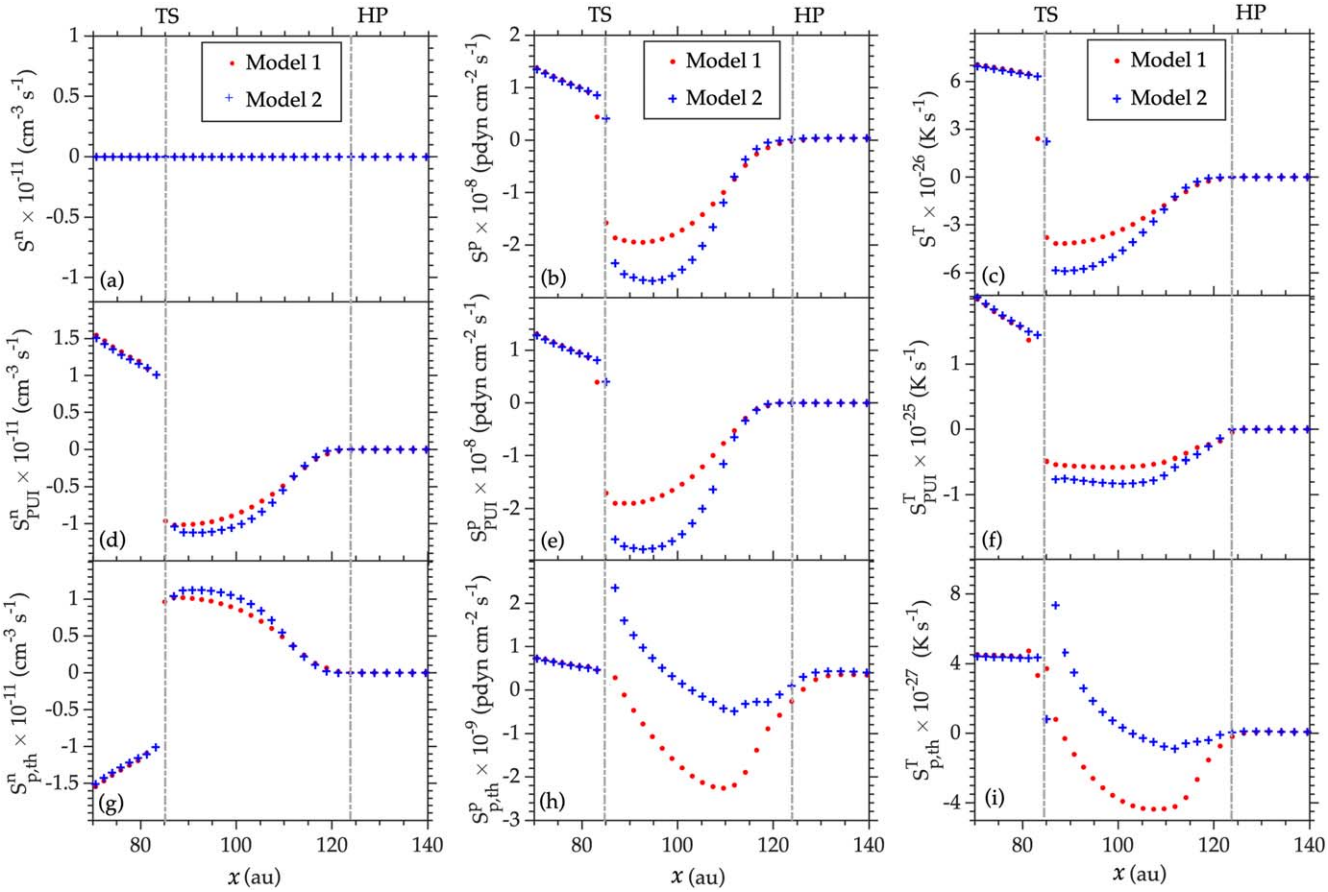

Figure 9. Distributions of the rate of change due to charge exchange for the proton density (S^n), plasma pressure (S^p), and plasma temperature (S^T) along the x-axis from 70 to 140 au in `Model 1` (red dots) and `Model 2` (blue plus symbols). From the top to the bottom, these quantities are shown for the plasma, PUIs, and thermal protons.

in Model 2, when the PUIs experience charge exchange. This analysis can be used as a proxy to calculate the ENA fluxes at 1 au, following a similar approach used by Heerikhuisen et al. (2019). Hence, the energy-averaged ENA fluxes at 1 au computed from `Model 2` are expected to be higher by ∼50%–60% as compared to `Model 1`. This does not mean, however, that this applies also to ENA fluxes in any particular energy band, because they are strongly dependent on the accepted distribution function for PUIs. For this reason, we cannot provide any direct comparison with the IBEX data.

Thus, the new model, which incorporates the results of the hybrid simulations of the mixture of thermal and nonthermal ions crossing the TS, may shed more light on the interpretation of the ENA fluxes observed by IBEX and provide improvements to the previous analyses (see, e.g., Zirnstein et al. 2017; Heerikhuisen et al. 2019; Shrestha et al. 2020). In addition to the advantage of using a more accurate energy partition between different populations of ions, the proposed approach is self-consistent.

6. Conclusions and Discussion

We have investigated the 3D SW–LISM interaction in which PUIs are treated as a separate fluid. In contrast to previous approaches, where the PUI properties in the IHS are derived a posteriori, our global model incorporates the boundary conditions for PUIs over the whole TS, which are derived from hybrid kinetic simulations. This allows us to obtain a self-consistent solution and describe the flow of PUIs in the IHS. As the fluid dynamics equations are not appropriate for the description of the highly anisotropic PUIs near the TS, the PUI temperature and pressure behind the TS have been found on the basis of numerous hybrid kinetic simulations. The results of these simulations, which covered a broad range of possible shock properties relevant to the TS, have been used to create a lookup table that served to find the PUI temperature and pressure immediately behind the TS. These values have been used in our global model, in which the flow of plasma is described magnetohydrodynamically, while the different populations of neutral atoms are treated with a multifluid approach. We have found an efficient way to parameterize the results of our hybrid simulations, which allowed us to determine the shock properties uniquely and avoid numerical artifacts associated with smearing of discontinuities typical of the shock-capturing approach. In particular, the downstream-to-upstream ratio of PUI temperatures across the shock was expressed in terms of only upstream parameters (θ_{Bn}, M_A, and plasma β). The flow of the ion–electron mixture was described with the system of equations written in the conservation-law form. This made it possible to use the local shock properties in determining the downstream temperature and pressure of PUIs.

To isolate the effect of PUIs, we assumed that the SW is spherically symmetric and stationary at 1 au, its properties being chosen as averages of OMNI data. The simulation results were validated by comparing with NH SWAP

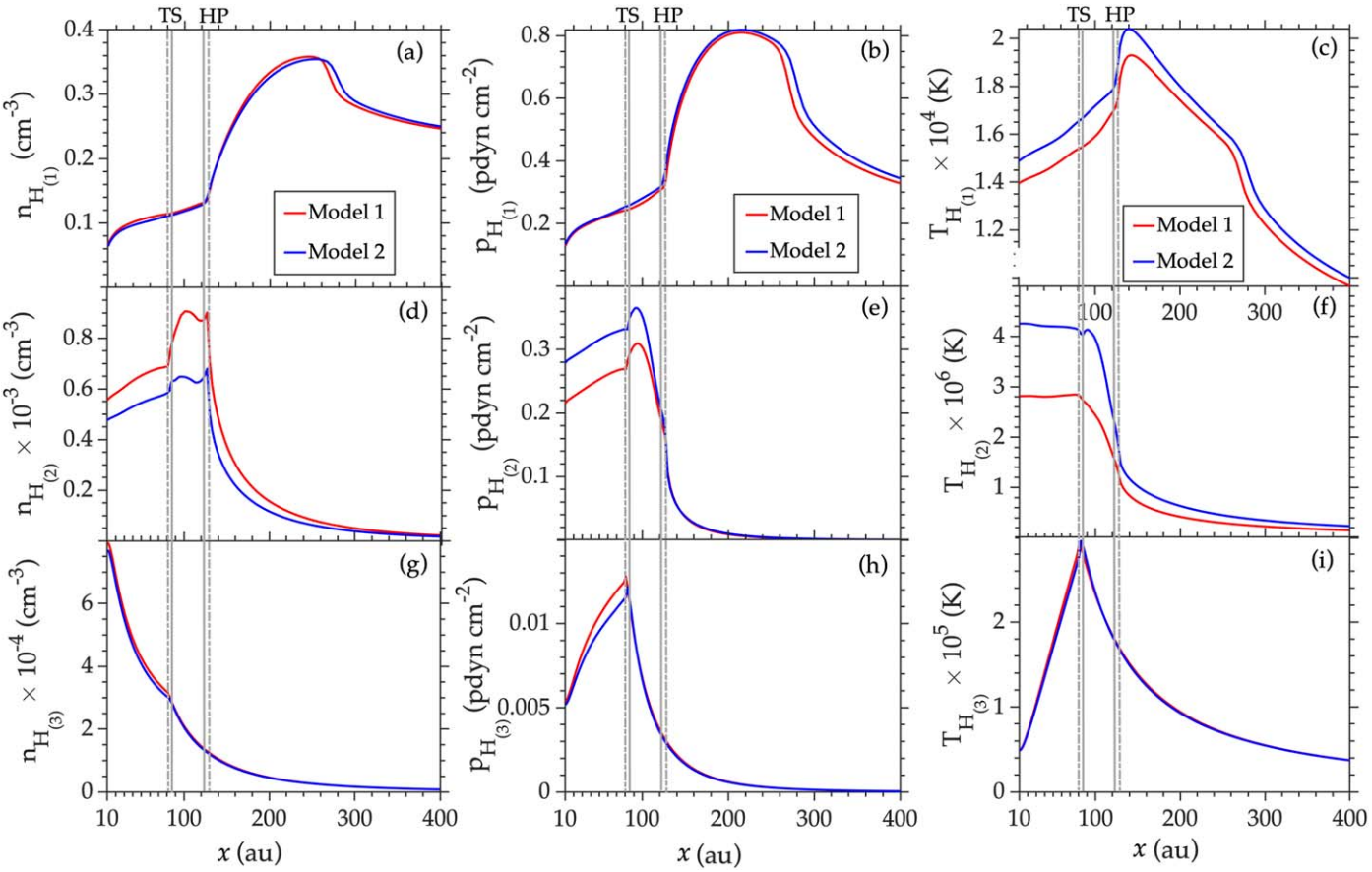

Figure 10. Distributions of the density, pressure, and temperature of neutral H atoms in `Model 1` (red lines) and `Model 2` (blue lines) along the *x*-axis from 10 to 400 au. The top, middle, and bottom panels refer to $H_{(1)}$, $H_{(2)}$, and $H_{(3)}$. The TS and HP are shown by the dashed and solid gray vertical lines for Models 1 and 2, respectively.

measurements of thermal protons and PUIs at radial distances between 11 and 47 au (from 2008 to 2020). The good performance of the model is also seen from a comparison with the V2 observations at distances from 10 to 80 au (1982–2006). The model accurately reproduces the average behavior and global radial trends in the distributions of thermal ions and PUIs. While the results of data-driven simulations will be presented elsewhere, there are strong and promising indications that our approach will be important in further interpreting NH data, as well as for the upcoming IMAP mission (McComas et al. 2018).

As shown, e.g., in Pogorelov et al. (2013) and Kim et al. (2017), the distributions in the IHS are strongly dependent on the temporal behavior of the solutions. For this reason, a meaningful comparison of simulation results with observations can be done only using data-driven boundary conditions. Moreover, our model, similarly to Opher et al. (2015), Pogorelov et al. (2017b), Korolkov & Izmodenov (2021), assumes a unipolar heliospheric magnetic field, which is known to dramatically exaggerate the HMF magnitude in the IHS, resulting in plasma beta values of the order of one near the HP, as shown in Figure 7 (see also Pogorelov et al. 2015, 2021). This is a likely explanation of the heliotail splitting into two lobes.

A major step forward has been made in the description of the SW flow in the outer heliosphere beyond the TS. Our simulation results demonstrate the accuracy of the proposed model in treating PUIs as they traverse the TS and propagate through the IHS. Considerable differences have been identified with respect to other, overly simplified approaches. In particular, we have shown that the IHS width becomes noticeably narrower with our PUI treatment and provided an explanation of this effect on the basis of a thorough inspection of the charge-exchange source terms, both in the equations we were solving and in the hypothetical ones, calculated to identify important properties of the multicomponent SW plasma. The PUI pressure and temperature in our new model (Model 2) based on the kinetically derived boundary conditions for PUIs at the TS are significantly higher (by ∼40%–50%) as compared with Model 1, in which the continuity and pressure equations for PUIs are solved throughout the heliosphere without paying attention to their kinetic behavior. The increase in PUI pressure results in a reduction of the thermal ion pressure. This leads to a significant changes in the charge-exchange probability for both PUIs and thermal protons, especially in the IHS. As a result, the overall plasma pressure in the IHS decreases and the plasma experiences additional cooling. The changes in the charge-exchange source terms have a notable impact on the flow of neutral atoms, in particular those that originate in the IHS. This ultimately leads to a reduction in the width of the IHS by 8–10 au in the upstream direction, and even more (about 60–80 au) in the downwind direction.

While this result may depend on the distribution function of plasma in the IHS (e.g., Lorentzian or multicomponent Maxwellian, Heerikhuisen et al. 2019), it should be understood

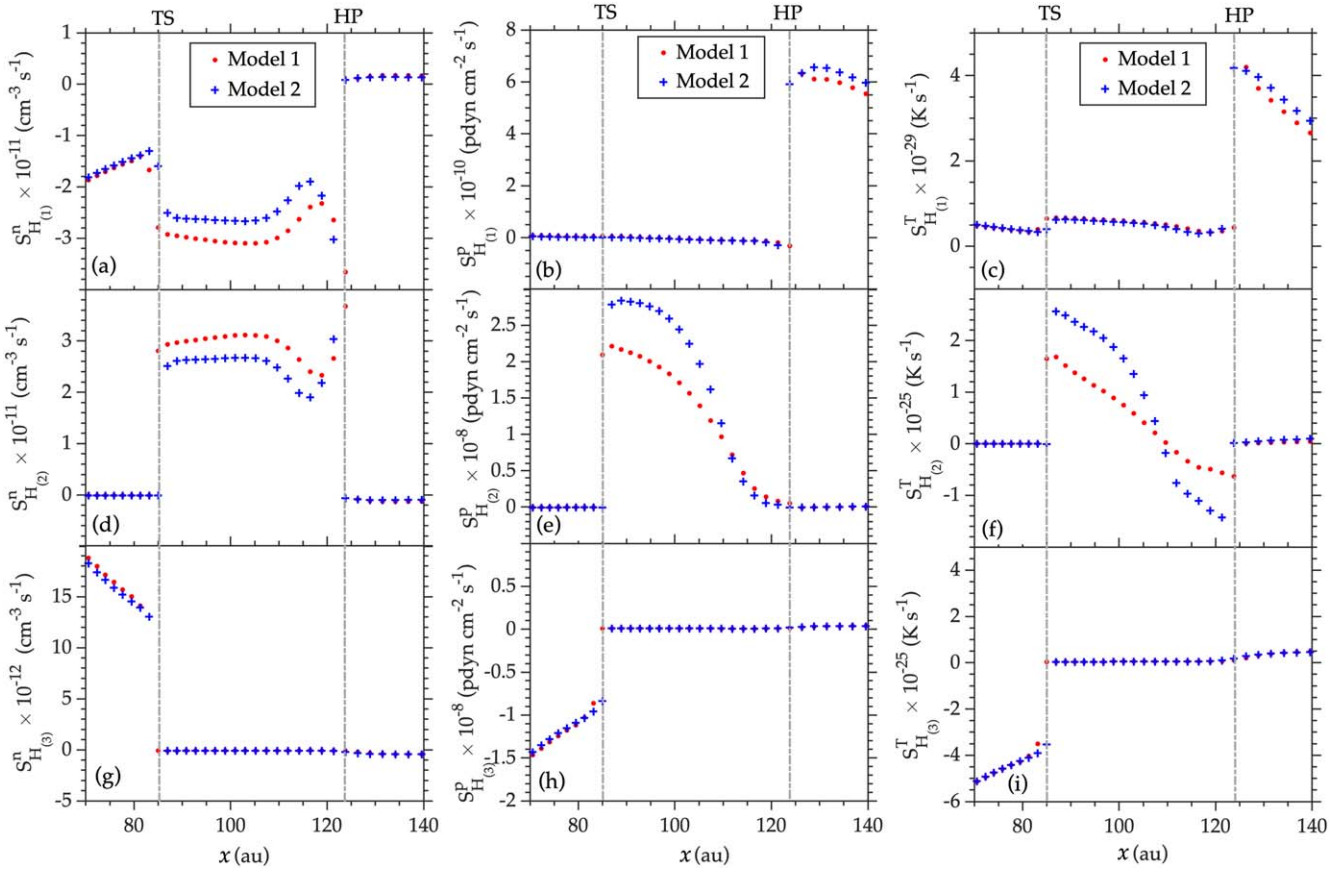

Figure 11. Distributions of source terms associated with the density, pressure, and temperature of neutral populations ($H_{(1)}$, $H_{(2)}$, and $H_{(3)}$) along the x-axis from 70 to 140 au in `Models 1` (red dots) and `2` (blue plus symbols). Top panels (a), (b), and (c) show $S^n_{H_{(1)}}$, $S^p_{H_{(1)}}$, and $S^T_{H_{(1)}}$ for $H_{(1)}$. The middle and bottom panels show the same quantities for $H_{(2)}$ and $H_{(3)}$.

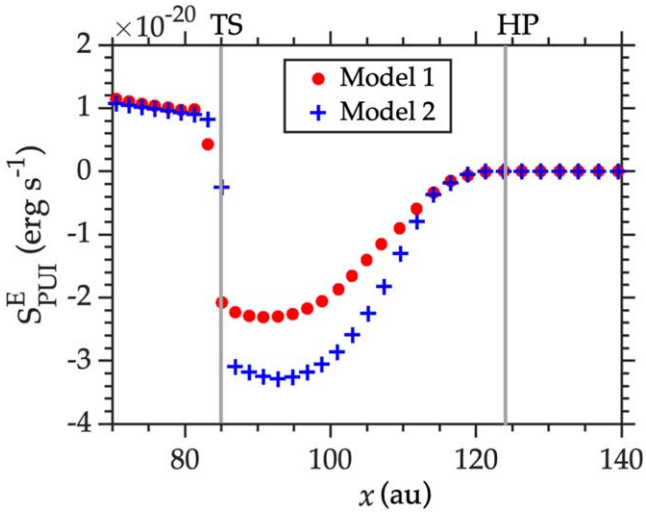

Figure 12. Distributions of source term associated with the evolution of PUI energy along the x-axis from 70 to 140 au in `Models 1` (red dots) and `2` (blue plus symbols).

that this width is time-dependent, with PUIs potentially playing a lesser role. The analysis of Pogorelov (2023), based on the data-driven simulations of Kim et al. (2017) and Pogorelov et al. (2021), has shown that even without special treatment of PUIs, the width in the V1 direction has been smaller than 43 au since 2014, reached 30 au in 2017, and remained nearly constant between 2019 and 2021.

We compared the PUI properties obtained in Model 2 with the theoretical approach of Zank et al. (2010b) and further extended by Heerikhuisen et al. (2019) and Shrestha et al. (2020). Our analysis shows that our model produces comparatively higher downstream PUI temperatures (∼7%–8%) in certain regions of the TS, e.g., at the TS flanks and poles. This effect is particularly pronounced in areas where the shock is more oblique, and it may therefore have important implications for time-dependent simulations where a wider range of shock angles is expected. On the contrary, the PUI temperature immediately after the TS in the upwind direction is somewhat lower. However, in contrast to other models where the energy separation between PUIs and thermal SW ions is taken into account, our model performs simulations both across the TS and in the IHS self-consistently.

The properties of PUIs and neutral atoms obtained with `Model 2` will be particularly important in the context of ENA modeling. Although we cannot determine the global ENA flux as a function of energy, our analysis shows that the energy-integrated ENA production increases, and more energetic ENAs are produced in `Model 2` as compared to `Model 1`. We note that Model 2 has a better physical basis because it includes a kinetic description of PUIs crossing the TS.

The proposed approach makes it possible to include time-dependent effects (e.g., solar cycle) and explore the global properties of the heliosphere in a way that can be directly validated by in situ measurements from the NH and IMAP missions. These results will be presented elsewhere.

Acknowledgments

This work is supported by NASA grants 80NSSC18K1212 and 80NSSC18K1649, and NSF-BSF grants 2010450, 2010144, and 2019744. It was also partially funded by the IBEX mission as part of NASA's Explorer Program (80NSSC18K0237) and IMAP mission as a part of NASA's Solar Terrestrial Probes (STP) Program (80GSFC19C0027). The authors acknowledge the Texas Advanced Computing Center (TACC) at The University of Texas at Austin for providing HPC resources on Frontera supported by NSF award CISE-OAC-2031611. Supercomputer time allocations were also provided by NASA High-End Computing Program award SMD-17-1537 and on Stampede 2 by ACCESS project MCA07S033.

Appendix

In this section, we present the charge-exchange chemical reactions considered in this study in the different regions of the heliosphere. As previously mentioned in Section 2, the heliosphere is divided into three subregions (labeled as Region 1, Region 2, and Region 3). The charge-exchange process in different regions is adapted from the work of Pogorelov et al. (2016). Here, we also summarize the reactions specific to each region below.

In Region 3 (supersonic SW):

$$\mathrm{H^+_{th}} + \mathrm{H_{(1)}} \rightarrow \mathrm{H^+_{PUI}} + \mathrm{H_{(3)}},\ \mathrm{H^+_{PUI}} + \mathrm{H_{(1)}} \rightarrow \mathrm{H^+_{PUI}} + \mathrm{H_{(3)}},$$

$$\mathrm{H^+_{th}} + \mathrm{H_{(2)}} \rightarrow \mathrm{H^+_{PUI}} + \mathrm{H_{(3)}},\ \mathrm{H^+_{PUI}} + \mathrm{H_{(2)}} \rightarrow \mathrm{H^+_{PUI}} + \mathrm{H_{(3)}},$$

$$\mathrm{H^+_{th}} + \mathrm{H_{(3)}} \rightarrow \mathrm{H^+_{th}} + \mathrm{H_{(3)}},\ \mathrm{H^+_{PUI}} + \mathrm{H_{(3)}} \rightarrow \mathrm{H^+_{th}} + \mathrm{H_{(3)}}.$$

In Region 2 (IHS):

$$\mathrm{H^+_{th}} + \mathrm{H_{(1)}} \rightarrow \mathrm{H^+_{th}} + \mathrm{H_{(2)}},\ \mathrm{H^+_{PUI}} + \mathrm{H_{(1)}} \rightarrow \mathrm{H^+_{th}} + \mathrm{H_{(2)}},$$

$$\mathrm{H^+_{th}} + \mathrm{H_{(2)}} \rightarrow \mathrm{H^+_{th}} + \mathrm{H_{(2)}},\ \mathrm{H^+_{PUI}} + \mathrm{H_{(2)}} \rightarrow \mathrm{H^+_{th}} + \mathrm{H_{(2)}},$$

$$\mathrm{H^+_{th}} + \mathrm{H_{(3)}} \rightarrow \mathrm{H^+_{th}} + \mathrm{H_{(2)}},\ \mathrm{H^+_{PUI}} + \mathrm{H_{(3)}} \rightarrow \mathrm{H^+_{th}} + \mathrm{H_{(2)}}.$$

In Region 1 (LISM):

$$\mathrm{H^+_{th}} + \mathrm{H_{(1),(2),(3)}} \rightarrow \mathrm{H^+_{th}} + \mathrm{H_{(1),(2),(3)}}.$$

For the sake of convenience in the following discussion, we use the subscripts c, I, and a to represent the core (thermal) SW protons, PUIs, and neutral atom populations, respectively. It is important to note that the variable a can assume the values 1, 2, and 3, which correspond to the populations of $\mathrm{H_{(1)}}$, $\mathrm{H_{(2)}}$, and $\mathrm{H_{(3)}}$, respectively. The following quantities are used in the definition of the source terms (Zank et al. 1996c):

$$U^{\rho}_{ij} = \left[\frac{4}{\pi}(v^2_{T_i} + v^2_{T_j}) + (\boldsymbol{u}_i - \boldsymbol{u}_j)^2\right]^{1/2}, \tag{A1}$$

$$U^{m}_{ij} = \left[\frac{16}{\pi}v^2_{T_i} + \frac{9\pi}{4}v^2_{T_j} + 4(\boldsymbol{u}_i - \boldsymbol{u}_j)^2\right]^{1/2}, \tag{A2}$$

$$U^{E}_{ij} = \left[\frac{4}{\pi}v^2_{T_i} + \frac{64}{9\pi}v^2_{T_j} + (\boldsymbol{u}_i - \boldsymbol{u}_j)^2\right]^{1/2}, \tag{A3}$$

$$\sigma_{\mathrm{ij}} = \sigma(U^{\rho}_{ij}) = (13.493 - 0.531\log U^{\rho}_{ij})^2 \times \left(1 - \exp\frac{-2.94\times 10^9}{U^{\rho}_{ij}}\right)^{4.5}. \tag{A4}$$

Here the subscripts i and j can have values of a and either c or I. The quantity v_T represents the thermal speed and σ_{ij} is the $H^+ + H$ charge-exchange cross section of particles of type i with particles of type j. The source terms are defined based on the following quantities:

$$H^{\rho}_{ak} = \sigma_{ak}\rho_k\rho_a U^{\rho}_{ak}, \qquad k = c, \mathrm{I}, \tag{A5}$$

$$\boldsymbol{H}^{m}_{ak} = \sigma_{ak}\rho_k\rho_a\left(U^{\rho}_{ak}\boldsymbol{u} + \frac{v^2_{T_k}}{U^{m}_{ak}}(\boldsymbol{u} - \boldsymbol{u}_a)\right), \tag{A6}$$

$$\boldsymbol{H}^{m}_{ka} = \sigma_{ka}\rho_k\rho_j\left(U^{\rho}_{ka}\boldsymbol{u}_a - \frac{v^2_{T_a}}{U^{m}_{ka}}(\boldsymbol{u} - \boldsymbol{u}_a)\right), \tag{A7}$$

$$H^{E}_{ak} = \sigma_{ak}\rho_k\rho_a\left(\frac{1}{2}u^2U^{\rho}_{ak} + \frac{3}{4}v^2_{T_k}U^{E}_{ak} + \frac{v^2_{T_k}}{U^{m}_{ak}}\boldsymbol{u}\cdot(\boldsymbol{u} - \boldsymbol{u}_a)\right), \tag{A8}$$

$$H^{E}_{ka} = \sigma_{ka}\rho_k\rho_a\left(\frac{1}{2}u^2_aU^{\rho}_{ka} + \frac{3}{4}v^2_{T_a}U^{E}_{ka} - \frac{v^2_{T_a}}{U^{m}_{ka}}\boldsymbol{u}_a\cdot(\boldsymbol{u} - \boldsymbol{u}_a)\right), \tag{A9}$$

$$H^{p}_{ak} = \sigma_{ak}\rho_k\rho_a(\gamma - 1)\frac{3}{4}v^2_{T_k}U^{E}_{ak}, \tag{A10}$$

$$H^{p}_{ka} = \sigma_{ka}\rho_k\rho_a(\gamma - 1)\left(\frac{1}{2}U^{\rho}_{ka}(\boldsymbol{u} - \boldsymbol{u}_a)^2 + \frac{v^2_{T_a}}{U^{m}_{ka}}(\boldsymbol{u} - \boldsymbol{u}_a)^2 + \frac{3}{4}v^2_{T_a}U^{E}_{ka}\right). \tag{A11}$$

The following relations are used to calculate the source terms for the PUI pressure equation:

$$H^{p}_{jk} = (\gamma - 1)\left(H^{E}_{jk} - \boldsymbol{u}\cdot\boldsymbol{H}^{m}_{jk} + \frac{1}{2}u^2H^{\rho}_{jk}\right),$$

$$H^{p}_{ak} = (\gamma - 1)\sigma_{ak}\frac{3}{4}v^2_{T_k}U^{E}_{ak}.$$

The source terms described in the Equations (1)–(9) have the following form at different regions.

Source terms in Region 3:

$$S^{\rho}_{\Sigma} = 0, \quad S^{\rho}_{\mathrm{H_{(1)}}} = -H^{\rho}_{\mathrm{c1}} - H^{\rho}_{\mathrm{I1}}, \quad S^{\rho}_{\mathrm{H_{(2)}}} = -H^{\rho}_{\mathrm{c2}} - H^{\rho}_{\mathrm{I2}},$$

$$S^{\rho}_{\mathrm{H_{(3)}}} = H^{\rho}_{\mathrm{c1}} + H^{\rho}_{\mathrm{c2}} + H^{\rho}_{\mathrm{I1}} + H^{\rho}_{\mathrm{I2}}, \quad S^{\rho}_{\mathrm{PUI}} = H^{\rho}_{\mathrm{c1}} + H^{\rho}_{\mathrm{c2}} - H^{\rho}_{\mathrm{I3}},$$

$$\boldsymbol{S}^{m}_{\Sigma} = -H^{m}_{\mathrm{1c}} + H^{m}_{\mathrm{c1}} - H^{m}_{\mathrm{2c}} + H^{m}_{\mathrm{c2}} - H^{m}_{\mathrm{3c}} + H^{m}_{\mathrm{c3}} - H^{m}_{\mathrm{1I}} + H^{m}_{\mathrm{I1}} - H^{m}_{\mathrm{2I}} + H^{m}_{\mathrm{I2}} - H^{m}_{\mathrm{3I}} + H^{m}_{\mathrm{I3}},$$

$$\boldsymbol{S}^{m}_{\mathrm{H_{(1)}}} = -H^{m}_{\mathrm{c1}} - H^{m}_{\mathrm{I1}}, \quad \boldsymbol{S}^{m}_{\mathrm{H_{(2)}}} = -H^{m}_{\mathrm{c2}} - H^{m}_{\mathrm{I2}},$$

$$\boldsymbol{S}^{m}_{\mathrm{H_{(3)}}} = -H^{m}_{\mathrm{c3}} + H^{m}_{\mathrm{3c}} + H^{m}_{\mathrm{1c}} + H^{m}_{\mathrm{2c}} - H^{m}_{\mathrm{I3}} + H^{m}_{\mathrm{3I}} + H^{m}_{\mathrm{1I}} + H^{m}_{\mathrm{2I}},$$

$$S^{E}_{\Sigma} = -H^{E}_{\mathrm{1c}} + H^{E}_{\mathrm{c1}} - H^{E}_{\mathrm{2c}} + H^{E}_{\mathrm{c2}} - H^{E}_{\mathrm{3c}} + H^{E}_{\mathrm{c3}} - H^{E}_{\mathrm{1I}} + H^{E}_{\mathrm{I1}} - H^{E}_{\mathrm{2I}} + H^{E}_{\mathrm{I2}} - H^{E}_{\mathrm{3I}} + H^{E}_{\mathrm{I3}},$$

$$S^{\mathrm{E}}_{\mathrm{H_{(1)}}} = -H^{E}_{\mathrm{c1}} - H^{E}_{\mathrm{I1}}, \quad S^{\mathrm{E}}_{2} = -H^{E}_{\mathrm{c2}} - H^{E}_{\mathrm{I2}},$$

$$S^{E}_{\mathrm{H_{(3)}}} = -H^{E}_{\mathrm{c3}} + H^{E}_{\mathrm{3c}} + H^{E}_{\mathrm{1c}} + H^{E}_{\mathrm{2c}} - H^{E}_{\mathrm{I3}} + H^{E}_{\mathrm{3I}} + H^{E}_{\mathrm{1I}} + H^{E}_{\mathrm{2I}},$$

$$S^{p}_{\mathrm{PUI}} = H^{p}_{\mathrm{c1}} + H^{p}_{\mathrm{c2}} + H^{p}_{\mathrm{I1}} - H^{p}_{\mathrm{I1}} + H^{\mathrm{p}}_{\mathrm{I2}} - H^{p}_{\mathrm{2I}} - H^{p}_{\mathrm{3I}}.$$

Source terms in Region 2:

$$S^{\rho}_{\Sigma} = 0, \; S^{\rho}_{\mathrm{H_{(1)}}} = -H^{\rho}_{\mathrm{c1}} - H^{\rho}_{\mathrm{I1}}, \quad S^{\rho}_{\mathrm{H_{(2)}}} = H^{\rho}_{\mathrm{c1}} + H^{\rho}_{\mathrm{c3}} + H^{\rho}_{\mathrm{I1}} + H^{\rho}_{\mathrm{I3}},$$

$$S^{\rho}_{\mathrm{H}_{(3)}} = -H^{\rho}_{\mathrm{c3}} - H^{\rho}_{\mathrm{I3}}, \quad S^{\rho}_{\mathrm{PUI}} = -H^{\rho}_{\mathrm{I1}} - H^{\rho}_{\mathrm{I2}} - H^{\rho}_{\mathrm{I3}},$$

$$\boldsymbol{S}^{m}_{\Sigma} = -H^{m}_{\mathrm{1c}} + H^{m}_{\mathrm{c1}} - H^{m}_{\mathrm{2c}} + H^{m}_{\mathrm{c2}} - H^{m}_{\mathrm{3c}} + H^{m}_{\mathrm{c3}} - H^{m}_{\mathrm{1I}} + H^{m}_{\mathrm{I1}} - H^{m}_{\mathrm{2I}} + H^{m}_{\mathrm{I2}} - H^{m}_{\mathrm{3I}} + H^{m}_{\mathrm{I3}},$$

$$\boldsymbol{S}^{m}_{\mathrm{H}_{(1)}} = -H^{m}_{\mathrm{c1}} - H^{m}_{\mathrm{I1}}, \quad \boldsymbol{S}^{m}_{\mathrm{H}_{(2)}} = -H^{m}_{\mathrm{c2}} + H^{m}_{\mathrm{2c}} + H^{m}_{\mathrm{1c}} + H^{m}_{\mathrm{3c}} - H^{m}_{\mathrm{I2}} + H^{m}_{\mathrm{2I}} + H^{m}_{\mathrm{1I}} + H^{m}_{\mathrm{3I}},$$

$$\boldsymbol{S}^{m}_{\mathrm{H}_{(3)}} = -H^{m}_{\mathrm{c3}} - H^{m}_{\mathrm{I3}},$$

$$S^{E}_{\Sigma} = -H^{E}_{\mathrm{1p}} + H^{E}_{\mathrm{c1}} - H^{E}_{\mathrm{2c}} + H^{E}_{\mathrm{c2}} - H^{E}_{\mathrm{3c}} + H^{E}_{\mathrm{c3}} - H^{E}_{\mathrm{1I}} + H^{E}_{\mathrm{I1}} - H^{E}_{\mathrm{2I}} + H^{E}_{\mathrm{I2}} - H^{E}_{\mathrm{3I}} + H^{E}_{\mathrm{I3}},$$

$$S^{E}_{\mathrm{H}_{(1)}} = -H^{E}_{\mathrm{c1}} - H^{E}_{\mathrm{I1}},$$

$$S^{E}_{\mathrm{H}_{(2)}} = -H^{E}_{\mathrm{c2}} + H^{E}_{\mathrm{2c}} + H^{E}_{\mathrm{1c}} + H^{E}_{\mathrm{3c}} - H^{E}_{\mathrm{I2}} + H^{E}_{\mathrm{2I}} + H^{E}_{\mathrm{1I}} + H^{E}_{\mathrm{3I}},$$

$$S^{E}_{\mathrm{H}_{(3)}} = -H^{E}_{\mathrm{c3}} - H^{E}_{\mathrm{I3}}, \quad S^{p}_{\mathrm{PUI}} = -H^{p}_{\mathrm{1I}} - H^{p}_{\mathrm{2I}} - H^{p}_{\mathrm{3I}}.$$

Source terms in Region 1:

$$S^{\rho}_{\Sigma} = 0, \quad S^{\rho}_{\mathrm{H}_{(1)}} = H^{\rho}_{\mathrm{c2}} + H^{\rho}_{\mathrm{c3}},$$

$$S^{\rho}_{\mathrm{H}_{(2)}} = -H^{\rho}_{\mathrm{c2}}, \quad S^{\rho}_{\mathrm{H}_{(3)}} = -H^{\rho}_{\mathrm{c3}}, \quad S^{\rho}_{\mathrm{PUI}} = 0,$$

$$\boldsymbol{S}^{m}_{\Sigma} = -H^{m}_{\mathrm{1c}} + H^{m}_{\mathrm{c1}} - H^{m}_{\mathrm{2c}} + H^{m}_{\mathrm{c2}} - H^{m}_{\mathrm{3c}} + H^{m}_{\mathrm{c3}},$$

$$\boldsymbol{S}^{m}_{\mathrm{H}_{(1)}} = -H^{m}_{\mathrm{c1}} + H^{m}_{\mathrm{1c}} + H^{m}_{\mathrm{2c}} + H^{m}_{\mathrm{3c}},$$

$$\boldsymbol{S}^{m}_{\mathrm{H}_{(2)}} = -H^{m}_{\mathrm{c2}}, \quad \boldsymbol{S}^{m}_{\mathrm{H}_{(3)}} = -H^{m}_{\mathrm{c3}},$$

$$S^{E}_{\Sigma} = -H^{E}_{\mathrm{1c}} + H^{E}_{\mathrm{c1}} - H^{E}_{\mathrm{2c}} + H^{E}_{\mathrm{c2}} - H^{E}_{\mathrm{3c}} + H^{E}_{\mathrm{c3}},$$

$$S^{E}_{\mathrm{H}_{(1)}} = -H^{E}_{\mathrm{c1}} + H^{E}_{\mathrm{1c}} + H^{E}_{\mathrm{2c}} + H^{E}_{\mathrm{3c}}, \quad S^{E}_{\mathrm{H}_{(2)}} = -H^{E}_{\mathrm{c2}}, \quad S^{E}_{\mathrm{H}_{(3)}} = -H^{E}_{\mathrm{c3}}, \quad S^{p}_{\mathrm{PUI}} = 0.$$

In the given expressions, the order of the subscript and sign varies depending on the reactions involved in different regions. For instance, in region 2, H^{m}_{I1} represents the source term contribution to the momentum equation resulting from the charge exchange between a population 1 ($\mathrm{H}_{(1)}$) neutral atom and a PUI. As described, charge exchange leads to the generation of a thermal proton and a $\mathrm{H}_{(2)}$ neutral atom. Hence, the term H^{m}_{I1} is subtracted from $\boldsymbol{S}^{\mathrm{m}}_{\mathrm{H}_{(1)}}$ and added to $\boldsymbol{S}^{\mathrm{m}}_{\Sigma}$. Similarly, H^{m}_{I1} represents the source term contribution to the momentum equation when a PUI charge exchange with a population 1 neutral atom, causing the PUI loss and the production of an $\mathrm{H}_{(2)}$ atom. Consequently, H^{m}_{I1} is subtracted from $\boldsymbol{S}^{\mathrm{m}}_{\Sigma}$ and added to $\boldsymbol{S}^{\mathrm{m}}_{\mathrm{H}_{(2)}}$.

ORCID iDs

R. K. Bera https://orcid.org/0000-0002-4207-3633
F. Fraternale https://orcid.org/0000-0002-4700-2762
N. V. Pogorelov https://orcid.org/0000-0002-6409-2392
V. Roytershteyn https://orcid.org/0000-0003-1745-7587
M. Gedalin https://orcid.org/0000-0003-1236-4787
D. J. McComas https://orcid.org/0000-0001-6160-1158
G. P. Zank https://orcid.org/0000-0002-4642-6192

References

Adhikari, L., Zank, G. P., Bruno, R., et al. 2015, ApJ, 805, 63
Adhikari, L., Zank, G. P., Hunana, P., & Hu, Q. 2016, ApJ, 833, 218
Ariad, D., & Gedalin, M. 2013, JGRA, 118, 2854
Balogh, A., Southwood, D. J., Forsyth, R. J., et al. 1995, Sci, 268, 1007
Baranov, V. B., & Malama, Y. G. 1993, JGR, 98, 15157
Borovikov, S. N., Heerikhuisen, J., & Pogorelov, N. V. 2013, in ASP Conf. Ser. 474, Numerical Modeling of Space Plasma Flows: Astronum-2012, ed. N. V. Pogorelov, E. Audit, & G. P. Zank (San Francisco, CA: ASP), 219
Borovikov, S. N., Kryukov, I. A., & Pogorelov, N. V. 2009, in ASP Conf. Ser. 406, Numerical Modeling of Space Plasma Flows: Astronum-2008, ed. N. V. Pogorelov et al. (San Francisco, CA: ASP), 127
Borovikov, S. N., Pogorelov, N. V., Burlaga, L. F., & Richardson, J. D. 2011, ApJL, 728, L21
Borovikov, S. N., Pogorelov, N. V., & Ebert, R. W. 2012, ApJ, 750, 42
Breech, B., Matthaeus, W. H., Minnie, J., et al. 2008, JGRA, 113, A08105
Burrows, R. H., Zank, G. P., Webb, G. M., Burlaga, L. F., & Ness, N. F. 2010, ApJ, 715, 1109
Bzowski, M., Czechowski, A., Frisch, P. C., et al. 2019, ApJ, 882, 60
Chalov, S. V., Alexashov, D. B., & Fahr, H. J. 2006, AstL, 32, 206
Chalov, S. V., & Fahr, H. J. 2000, A&A, 360, 381
Chalov, S. V., Malama, Y. G., Alexashov, D. B., & Izmodenov, V. V. 2015, MNRAS, 455, 431
Decker, R. B., Krimigis, S. M., Roelof, E. C., et al. 2008, Natur, 454, 67
Decker, R. B., Krimigis, S. M., Roelof, E. C., & Hill, M. E. 2015, JPhCS, 577, 012006
DeStefano, A. M., & Heerikhuisen, J. 2017, JPhCS, 837, 012013
DeStefano, A. M., & Heerikhuisen, J. 2020, PhPl, 27, 032901
Elliott, H. A., McComas, D. J., Valek, P., et al. 2016, ApJS, 223, 19
Elliott, H. A., McComas, D. J., Zirnstein, E. J., et al. 2019, ApJ, 885, 156
Fraternale, F., Adhikari, L., Fichtner, H. F., et al. 2022, SSRv, 218, 75
Fraternale, F., Pogorelov, N. V., & Bera, R. K. 2023, ApJ, 946, 97
Fraternale, F., Pogorelov, N. V., & Heerikhuisen, J. 2021, ApJL, 921, L24
Galeev, A. A., & Sagdeev, R. Z. 1988, Ap&SS, 144, 427
Gamayunov, K. V., Zhang, M., Pogorelov, N. V., Heerikhuisen, J., & Rassoul, H. K. 2012, ApJ, 757, 74
Gedalin, M., Balikhin, M., & Krasnosselskikh, V. 1995, AdSpR, 15, 225
Gedalin, M., Dröge, W., & Kartavykh, Y. Y. 2016, ApJ, 825, 149
Gedalin, M., Golan, M., Pogorelov, N. V., & Roytershteyn, V. 2022, ApJ, 940, 21
Gedalin, M., Pogorelov, N. V., & Roytershteyn, V. 2021a, ApJ, 910, 107
Gedalin, M., Pogorelov, N. V., & Roytershteyn, V. 2021b, ApJ, 916, 57
Gedalin, M., Roytershteyn, V., & Pogorelov, N. V. 2023, ApJ, 945, 50
Geiss, J., Gloeckler, G., & Mall, U. 1994, A&A, 289, 933
Giacalone, J., Nakanotani, M., Zank, G. P., et al. 2021, ApJ, 911, 27
Heerikhuisen, J., Gamayunov, K. V., Zirnstein, E. J., & Pogorelov, N. V. 2016, ApJ, 831, 137
Heerikhuisen, J., & Pogorelov, N. V. 2011, ApJ, 738, 29
Heerikhuisen, J., Pogorelov, N. V., Zank, G. P., et al. 2010, ApJL, 708, L126
Heerikhuisen, J., Zirnstein, E. J., Pogorelov, N. V., Zank, G. P., & Desai, M. 2019, ApJ, 874, 76
Isenberg, P. A. 1986, JGR, 91, 9965
Isenberg, P. A. 2005, ApJ, 623, 502
Isenberg, P. A., Smith, C. W., & Matthaeus, W. H. 2003, ApJ, 592, 564
Isenberg, P. A., Smith, C. W., Matthaeus, W. H., & Richardson, J. D. 2010, ApJ, 719, 716
Isenberg, P. A., Vasquez, B. J., & Smith, C. W. 2023, ApJ, 944, 84
Kim, T., Kryukov, I., Pogorelov, N., Elliott, H., & Zank, G. P. 2018, ESS Open Archive, doi:10.1002/essoar.b60497724eca58de.7c985d5380f54d2b.1
Kim, T. K., Pogorelov, N. V., & Burlaga, L. F. 2017, ApJL, 843, L32
Kim, T. K., Pogorelov, N. V., Zank, G. P., Elliott, H. A., & McComas, D. J. 2016, ApJL, 832, 72
Kleimann, J., Dialynas, K., Fraternale, F., et al. 2022, SSRv, 218, 36
Kornbleuth, M., Opher, M., Dialynas, K., et al. 2023, ApJL, 945, L15
Korolkov, S., & Izmodenov, V. 2021, MNRAS, 504, 4589
Kryukov, I. A., Pogorelov, N. V., Zank, G. P., & Borovikov, S. N. 2012, in AIP Conf. Proc. 1436, Physics of the Heliosphere: A 10 Year Retrospective, ed. J. Heerikhuisen (Melville, NY: AIP), 48
Kulikovskii, A. G., Pogorelov, N. V., & Semenov, A. Y. 2000, Mathematical Aspects of Numerical Solution of Hyperbolic Systems (London: Chapman & Hall/CRC)
Kumar, R., Zirnstein, E. J., & Spitkovsky, A. 2018, ApJ, 860, 156
le Roux, J. A., Webb, G. M., Florinski, V., & Zank, G. P. 2007, ApJ, 662, 350
Lee, M. A., & Ip, W. H. 1987, JGR, 92, 11041
Linde, T. J., Gombosi, T. I., Roe, P. L., Powell, K. G., & DeZeeuw, D. L. 1998, JGR, 103, 1889
Lindsay, B. G., & Stebbings, R. F. 2005, JGRA, 110, A12213
Malama, Y. G., Izmodenov, V. V., & Chalov, S. V. 2006, A&A, 445, 693
Matsukiyo, S., Noumi, T., Zank, G. P., Washimi, H., & Hada, T. 2019, ApJ, 888, 11
Matthaeus, W. H., Zank, G. P., Smith, C. W., & Oughton, S. 1999, PvRvL, 82, 3444
McComas, D., Allegrini, F., Bagenal, F., et al. 2008, SSRv, 140, 261

McComas, D. J., Alexashov, D., Bzowski, M., et al. 2012, Sci, 336, 1291
McComas, D. J., Allegrini, F., Bochsler, P., et al. 2009a, SSRv, 146, 11
McComas, D. J., Allegrini, F., Bochsler, P., et al. 2009b, Sci, 326, 959
McComas, D. J., Bzowski, M., Fuselier, S. A., et al. 2015, ApJS, 220, 22
McComas, D. J., Christian, E. R., Schwadron, N. A., et al. 2018, SSRv, 214, 116
McComas, D. J., Swaczyna, P., Szalay, J. R., et al. 2021, ApJS, 254, 19
McComas, D. J., Zirnstein, E. J., Bzowski, M., et al. 2017, ApJS, 233, 8
Möbius, E., Hovestadt, D., & Klecker, B. 1985, Natur, 318, 426
Opher, M., Drake, J. F., Zieger, B., & Gombosi, T. I. 2015, ApJL, 800, L28
Opher, M., Loeb, A., Drake, J., & Toth, G. 2020, NatAs, 4, 675
Parker, E. 1965, P&SS, 13, 9
Pogorelov, N. V. 2023, in IAU Symp. 362, Predictive Power of Computational Astrophysics as a Discovery Tool, ed. D. Bisikalo, D. Wiebe, & C. Boily (San Francisco, CA: ASP), 309
Pogorelov, N. V., Bedford, M. C., Kryukov, I. A., & Zank, G. P. 2016, JPhCS, 767, 012020
Pogorelov, N. V., Borovikov, S., Heerikhuisen, J., et al. 2014, in Proc. 2014 Annual Conf. on Extreme Science and Engineering Discovery Environment XSEDE'14 (New York: ACM),
Pogorelov, N. V., Borovikov, S. N., Heerikhuisen, J., Kryukov, I. A., & Zank, G. P. 2010, in ASP Conf. Ser. 429, Numerical Modeling of Space Plasma Flows: Astronum-2009, ed. N. V. Pogorelov, E. Audit, & G. P. Zank (San Francisco, CA: ASP), 266
Pogorelov, N. V., Borovikov, S. N., Heerikhuisen, J., & Zhang, M. 2015, ApJL, 812, L6
Pogorelov, N. V., Borovikov, S. N., Zank, G. P., et al. 2012, ApJL, 750, L4
Pogorelov, N. V., Borovikov, S. N., Zank, G. P., & Ogino, T. 2009a, ApJ, 696, 1478
Pogorelov, N. V., Fichtner, H., Czechowski, A., et al. 2017a, SSRv, 212, 193
Pogorelov, N. V., Fraternale, F., Kim, T. K., Burlaga, L. F., & Gurnett, D. A. 2021, ApJL, 917, L20
Pogorelov, N. V., Heerikhuisen, J., Roytershteyn, V., et al. 2017b, ApJ, 845, 9
Pogorelov, N. V., Heerikhuisen, J., Zank, G., & Borovikov, S. N. 2009b, SSRv, 143, 31
Pogorelov, N. V., & Semenov, A. Y. 1997, A&A, 321, 330
Pogorelov, N. V., Suess, S. T., Borovikov, S. N., et al. 2013, ApJ, 772, 2
Pogorelov, N. V., Zank, G. P., & Ogino, T. 2006, ApJ, 644, 1299
Reisenfeld, D. B., Bzowski, M., Funsten, H. O., et al. 2021, ApJS, 254, 40
Richardson, J. D., Burlaga, L. F., Elliott, H., et al. 2022, SSRv, 218, 35
Richardson, J. D., Kasper, J. C., Wang, C., Belcher, J. W., & Lazarus, A. J. 2008, Natur, 454, 63
Richardson, J. D., Paularena, K. I., Lazarus, A. J., & Belcher, J. W. 1995, GeoRL, 22, 1469
Richardson, J. D., Phillips, J. L., Smith, C. W., & Gray, P. C. 1996, GeoRL, 23, 3259
Richardson, J. D., & Smith, C. W. 2003, GeoRL, 30, 1206
Shrestha, B. L., Zirnstein, E. J., & Heerikhuisen, J. 2020, ApJ, 894, 102
Smith, C. W., Hamilton, K., Vasquez, B. J., & Leamon, R. J. 2006, ApJL, 645, L85
Smith, C. W., Matthaeus, W. H., Zank, G. P., et al. 2001, JGR, 106, 8253
Sokół, J. M., Kucharek, H., Baliukin, I. I., et al. 2022, SSRv, 218, 18
Swaczyna, P., McComas, D. J., Zirnstein, E. J., et al. 2020, ApJ, 903, 48
Swaczyna, P., Rahmanifard, F., Zirnstein, E. J., McComas, D. J., & Heerikhuisen, J. 2021, ApJL, 911, L36
Usmanov, A. V., & Goldstein, M. L. 2006, JGRA, 111, A07101
Usmanov, A. V., Goldstein, M. L., & Matthaeus, W. H. 2016, ApJ, 820, 17
Vasyliunas, V. M., & Siscoe, G. L. 1976, JGR, 81, 1247
Wallis, M. 1971, NPhS, 233, 23
Wang, B., Zank, G. P., Shrestha, B. L., Kornbleuth, M., & Opher, M. 2023, ApJ, 944, 198
Wang, C., & Richardson, J. D. 2001, JGR, 106, 29401
Williams, L. L., & Zank, G. P. 1994, JGR, 99, 19229
Williams, L. L., Zank, G. P., & Matthaeus, W. H. 1995, JGR, 100, 17059
Zank, G. 2015, ARA&A, 53, 449
Zank, G. P. 1999, SSRv, 89, 413
Zank, G. P., Adhikari, L., Zhao, L.-L., et al. 2018, ApJ, 869, 23
Zank, G. P., Heerikhuisen, J., Pogorelov, N. V., Burrows, R., & McComas, D. 2010a, ApJ, 708, 1092
Zank, G. P., Heerikhuisen, J., Pogorelov, N. V., et al. 2013, ApJ, 763, 20
Zank, G. P., Hunana, P., Mostafavi, P., & Goldstein, M. L. 2014, ApJ, 797, 87
Zank, G. P., Kryukov, I. A., Pogorelov, N. V., & Shaikh, D. 2010b, in AIP Conf. Proc. 1216, 12th Int. Solar Wind Conf., ed. M. Maksimovic et al. (Melville, NY) 563
Zank, G. P., Matthaeus, W. H., & Smith, C. W. 1996a, JGR, 101, 17093
Zank, G. P., Pauls, H. L., Cairns, I. H., & Webb, G. M. 1996b, JGR, 101, 457
Zank, G. P., Pauls, H. L., Williams, L. L., & Hall, D. T. 1996c, JGR, 101, 21639
Zank, G. P., Sterken, V., Giacalone, J., et al. 2022, SSRv, 218, 34
Zhang, M., Pogorelov, N. V., Zhang, Y., Hu, H. B., & Schlickeiser, R. 2020, ApJ, 889, 97
Zilbersher, D., & Gedalin, M. 1997, P&SS, 45, 693
Zirnstein, E. J., Dayeh, M. A., Heerikhuisen, J., McComas, D. J., & Swaczyna, P. 2021, ApJS, 252, 26
Zirnstein, E. J., Heerikhuisen, J., Funsten, H. O., et al. 2016, ApJL, 818, L18
Zirnstein, E. J., Heerikhuisen, J., Zank, G. P., et al. 2017, ApJ, 836, 238
Zirnstein, E. J., Shrestha, B. L., McComas, D. J., et al. 2022, NatAs, 6, 1398